

1 **A LINEAR-COMPLEXITY TENSOR BUTTERFLY ALGORITHM**
2 **FOR COMPRESSING HIGH-DIMENSIONAL OSCILLATORY**
3 **INTEGRAL OPERATORS**

4 P. MICHAEL KIELSTRA*, TIANYI SHI†, HENGRUI LUO ‡, JIANLIANG QIAN §, AND
5 YANG LIU†

6 **Abstract.** This paper presents a multilevel tensor compression algorithm called tensor butterfly
7 algorithm for efficiently representing large-scale and high-dimensional oscillatory integral operators,
8 including Green’s functions for wave equations and integral transforms such as Radon transforms
9 and Fourier transforms. The proposed algorithm leverages a tensor extension of the so-called com-
10plementary low-rank property of existing matrix butterfly algorithms. The algorithm partitions the
11discretized integral operator tensor into subtensors of multiple levels, and factorizes each subtensor
12at the middle level as a Tucker-type interpolative decomposition, whose factor matrices are formed in
13a multilevel fashion. For a d -dimensional ($d > 1$) integral operator discretized into a $2d$ -mode tensor
14with n^{2d} entries, the overall CPU time and memory requirement scale as $O(n^d)$, in stark contrast
15to the $O(n^d \log n)$ complexity of existing matrix algorithms such as matrix butterfly algorithms and
16fast Fourier transforms (FFT), where n is the number of points per direction. When comparing with
17other tensor algorithms such as quantized tensor train (QTT), the proposed algorithm also shows
18superior CPU and memory performance for tensor contraction. Remarkably, the tensor butterfly
19algorithm can efficiently model high-frequency Green’s function interactions between two unit cubes,
20each spanning 512 wavelengths per direction, which represent problems of scale over $512\times$ larger
21than that existing butterfly algorithms can handle, with the same amount of computation resources.
22On the other hand, for a problem representing 64 wavelengths per direction, which is the largest size
23existing algorithms can handle, our tensor butterfly algorithm exhibits $200\times$ speedups and $30\times$ mem-
24ory reduction comparing with existing ones. Moreover, the tensor butterfly algorithm also permits
25 $O(n^d)$ -complexity FFTs and Radon transforms up to $d = 6$ dimensions.

26 **Key word.** butterfly algorithm, tensor algorithm, Tucker decomposition, interpolative decom-
27position, quantized tensor train (QTT), fast Fourier transforms (FFT), fast algorithm, high-frequency
28wave equations, integral transforms, Radon transform, low-rank compression, Fourier integral oper-
29ator, non-uniform FFT (NUFFT)

30 **AMS subject classifications.** 15A23, 65F50, 65R10, 65R20

31 **1. Introduction.** Oscillatory integral operators (OIOs), such as Fourier trans-
32forms and Fourier integral operators [32, 7], are critical computational and theoretical
33tools for many scientific and engineering applications, such as signal and image pro-
34cessing, inverse problems and imaging, computer vision, quantum mechanics, and
35analyzing and solving partial differential equations (PDEs). The development of ac-
36curate and efficient algorithms for computing OIOs has profound impacts on the
37evolution of the pertinent research areas including, perhaps mostly remarkably, the
38invention of the fast Fourier transform (FFT) by Cooley and Tukey in 1965 and the
39invention of the fast multipole method (FMM) by Greengard and Rokhlin in 1987,
40both of which were listed among the ten most significant algorithms discovered in the
4120th century. Among existing analytical and algebraic methods for OIOs, butterfly al-
42gorithms [53, 47, 37, 36, 58] represent an emerging class of multilevel matrix decompo-

*Department of Mathematics, University of California, Berkeley, CA, USA.
Email: pmkielstra@berkeley.edu

†Applied Mathematics and Computational Research Division, Lawrence Berkeley National Lab-
oratory, Berkeley, CA, USA.

Email: {tianyishi, liuyangzhuang}@lbl.gov

‡Department of Statistics, Rice University, Houston, TX, USA. Email: hrluo@rice.edu

§Department of Mathematics and Department of CMSE, Michigan State University, East Lansing,
MI, USA. Email: jqian@msu.edu

43 sition algorithms that have been proposed for Fourier transforms and Fourier integral
 44 operators [8, 70, 69], special function transforms [65, 4, 56], fast iterative [54, 53, 48]
 45 and direct [24, 43, 25, 26, 61, 44, 62] solution of surface and volume integral equations
 46 for wave equations, high-frequency Green’s function ansatz for inhomogeneous wave
 47 equations [45, 41, 49], direct solution of PDE-induced sparse systems [42, 13], and
 48 machine learning for inverse problems [33, 35]. The (matrix) butterfly algorithms
 49 leverage the so-called complementary low-rank (CLR) property of the matrix repre-
 50 sentation of OIOs after proper row/column permutation. The CLR states that any
 51 submatrix with contiguous row and column index sets exhibits a low numerical rank
 52 if the number of the submatrix entries approximately equals the matrix size. These
 53 ranks are known as the butterfly ranks, which stay constant irrespective of the ma-
 54 trix sizes. This permits a multilevel sparse matrix decomposition requiring $O(n \log n)$
 55 factorization time, application time, and storage units with n being the matrix size.

56 Despite their low asymptotic complexity, the matrix butterfly algorithms often-
 57 times exhibit relatively large prefactors, i.e., constant but high butterfly ranks, par-
 58 ticularly for higher-dimensional OIOs. Examples include Green’s functions for 3D
 59 high-frequency wave equations [61, 45], 3D Radon transforms for linear inverse prob-
 60 lems [17], 6D Fourier–Bros–Iagolnitzer transforms for Wigner equations [15, 68], 6D
 61 Fourier transforms in diffusion magnetic resonance imaging [11] and plasma physics
 62 [18], 4D space-time transforms in quantum field theories [59, 50], and multi-particle
 63 Green’s functions in quantum chemistry [21]. For these high-dimensional OIOs, the
 64 computational advantage of the matrix butterfly algorithms over other existing algo-
 65 rithms becomes significant only for very large matrices.

66 More broadly speaking, for large-scale multi-dimensional scientific data and op-
 67 erators, tensor algorithms are typically more efficient than matrix algorithms. Popu-
 68 lar low-rank tensor compression algorithms include CANDECOMP/PARAFAC [30],
 69 Tucker [16], hierarchical Tucker [28], tensor train (TT) [57], and tensor network [12]
 70 decomposition algorithms. See references [34, 23] for a more complete review of
 71 available tensor formats and their applications. When applied to the representa-
 72 tion of high-dimensional integral operators, tensor algorithms often leverage addi-
 73 tional translational- or scaling-invariance property to achieve superior compression
 74 performance, including solution of quasi-static wave equations [67, 66, 22, 14], elliptic
 75 PDEs [3, 27], many-body Schrödinger equations [31], and quantum Fourier trans-
 76 forms (QFTs) [9]. That being said, most existing tensor decomposition algorithms
 77 will break down for OIOs due to their incapability to exploit the oscillatory structure
 78 of these operators; therefore, new tensor algorithms are called for.

79 In this paper, we propose a linear-complexity, low-prefactor tensor decomposi-
 80 tion algorithm for large-scale and high-dimensional OIOs. This new tensor algorithm,
 81 henceforth dubbed the tensor butterfly algorithm, leverages the intrinsic CLR prop-
 82 erty of high-dimensional OIOs more effectively than the matrix butterfly algorithm,
 83 which is enabled by additional tensor properties such as translational invariance of
 84 free-space Green’s functions and dimensional separability of Fourier transforms. The
 85 algorithm partitions the OIO tensor into subtensors of multiple levels, and factor-
 86 izes each subtensor at the middle level as a Tucker-type interpolative decomposition,
 87 whose factor matrices are further constructed in a nested fashion. For a d -dimensional
 88 OIO (assuming a constant $d > 1$) discretized as a $2d$ -mode tensor with n being the size
 89 per mode, the factorization time, application time, and storage cost scale as $O(n^d)$,
 90 and the resulting tensor factors have small multi-linear ranks. This is in stark contrast
 91 both to the $O(n^d \log n)$ scaling of existing matrix algorithms such as matrix butterfly
 92 algorithms and FFTs, and to the super-linear scaling of existing tensor algorithms. We

93 mention that the linear complexity of the factorization time in our proposed algorithm
 94 is achieved via a simple random entry evaluation scheme, assuming that any arbitrary
 95 entry can be computed in $O(1)$ time. We remark that, for 3D high-frequency wave
 96 equations, the proposed tensor butterfly algorithm can handle $512\times$ larger discretized
 97 Green’s function tensors than existing butterfly algorithms using the same amount
 98 of computation resources; on the other hand, for the largest sized tensor that can
 99 be handled by existing butterfly algorithms, our tensor butterfly algorithm is $200\times$
 100 faster than existing ones. Moreover, we claim that the tensor butterfly algorithm
 101 instantiates the first linear-complexity implementation of high-dimensional FFTs for
 102 arbitrary input data.

103 **1.1. Related Work.** *Multi-dimensional butterfly algorithms* represent a version
 104 of matrix butterfly algorithms designed for high-dimensional OIOs [38, 10]. Instead
 105 of the traditional binary tree partitioning of the matrix rows/columns [53], these
 106 algorithms can be viewed as a modern version of [54] that permits quadtree and octree
 107 partitioning of the matrix rows/columns, which have been demonstrated on 2D and
 108 3D OIOs. For a general d -dimensional OIO, the d -dimensional tree partitioning leads
 109 to a butterfly factorization with a d -fold reduction in the number of levels compared
 110 to the binary tree partitioning. That said, the binary tree based butterfly algorithms
 111 are easier to implement and exhibit very competitive overall costs comparing with the
 112 multi-dimensional butterfly algorithms. We note that both the multi-dimensional and
 113 binary tree-based butterfly algorithms are still matrix-based algorithms that scale as
 114 $O(n^d \log n)$, as opposed to the proposed tensor algorithm that scales as $O(n^d)$.

115 *Quantized tensor train (QTT) algorithms*, or simply TT algorithms, are tensor
 116 algorithms well-suited for very high-dimensional integral operators. They have been
 117 proposed to compress volume integral operators [14] arising from quasi-static wave
 118 equations and static PDEs with $O(\log n)$ memory and CPU complexities. However,
 119 for high-frequency wave equations, the QTT rank scales proportionally to the wave
 120 number [14] leading to deteriorated CPU and memory complexities (see our numerical
 121 results in Section section 4). Moreover, QTT has been proposed for computing FFT
 122 and QFT with $O(\log n)$ memory and CPU complexities [9]. However, after obtaining
 123 the QTT-compressed formats of both the volume-integral operator and the Fourier
 124 transform, the CPU complexity for contracting such a QTT compressed operator with
 125 arbitrary (i.e., non QTT-compressed) input data scales super-linearly. In contrast, our
 126 algorithm yields a linear CPU and memory complexity for the contraction operation.

127 **1.2. Contents.** In what follows, we first review the matrix low-rank decompo-
 128 sition and butterfly decomposition algorithms in section 2. In subsection 3.1, we in-
 129 troduce the Tucker-type interpolative decomposition algorithm as the building block
 130 for the proposed tensor butterfly algorithm detailed in subsection 3.2. The multi-
 131 linear butterfly ranks for a few special cases are analyzed in subsection 3.2.1 and the
 132 complete complexity analysis is given in subsection 3.2.2. Section 4 shows a variety
 133 of numerical examples, including Green’s functions for wave equations, Radon trans-
 134 forms, and uniform and non-uniform discrete Fourier transforms, to demonstrate the
 135 performance of matrix butterfly, tensor butterfly, Tucker and QTT algorithms.

136 **1.3. Notations.** Given a scalar-valued function $f(x)$, its integral transform is
 137 defined as

138 (1.1)
$$g(x) = \int_y K(x, y) f(y) dy$$

139 with an integral kernel $K(x, y)$. The indexing of a matrix \mathbf{K} is denoted by $\mathbf{K}(i, j)$
 140 or $\mathbf{K}(t, s)$, where i, j are indices and t, s are index sets. We use \mathbf{K}^T to denote the
 141 transpose of matrix \mathbf{K} . For a sequence of matrices $\mathbf{K}_1, \dots, \mathbf{K}_n$, the matrix product is

$$142 \quad (1.2) \quad \prod_{i=1}^n \mathbf{K}_i = \mathbf{K}_1 \mathbf{K}_2 \dots \mathbf{K}_n,$$

143 the vertical stacking (assuming the same column dimension) is

$$144 \quad (1.3) \quad [\mathbf{K}_i]_i = [\mathbf{K}_1; \mathbf{K}_2; \dots; \mathbf{K}_n],$$

145 and

$$146 \quad (1.4) \quad \text{diag}_i(\mathbf{K}_i) = \text{diag}(\mathbf{K}_1, \mathbf{K}_2, \dots, \mathbf{K}_n)$$

147 is a block diagonal matrix with \mathbf{K}_i being the diagonal blocks. Given an L -level binary-
 148 tree partitioning \mathcal{T}_t of an index set $t = \{1, 2, \dots, n\}$, any node τ at each level is a subset
 149 of t . The parent and children of τ are denoted by p_τ and τ^c ($c = 1, 2$), respectively,
 150 and $\tau = \tau^1 \cup \tau^2$.

151 A multi-index $\mathbf{i} = (i_1, \dots, i_d)$ is a tuple of indices, and similarly a multi-set
 152 $\boldsymbol{\tau} = (\tau_1, \tau_2, \dots, \tau_d)$ is a tuple of index sets. We define

$$153 \quad (1.5) \quad \boldsymbol{\tau}_{k \leftarrow t} = (\tau_1, \tau_2, \dots, \tau_{k-1}, t, \tau_{k+1}, \tau_{k+2}, \dots, \tau_d).$$

154 Given a tuple of nodes (i.e. a multi-set) $\boldsymbol{\tau} = (\tau_1, \tau_2, \dots, \tau_d)$ and a multi-index $\mathbf{c} =$
 155 (c_1, c_2, \dots, c_d) with $c_i \in \{1, 2\}$, the children of $\boldsymbol{\tau}$ are denoted $\boldsymbol{\tau}^{\mathbf{c}} = (\tau_1^{c_1}, \tau_2^{c_2}, \dots, \tau_d^{c_d})$
 156 and the parents of τ_i , $i = 1, 2, \dots, d$ can be simply written as $\mathbf{p}_\boldsymbol{\tau} = (p_{\tau_1}, p_{\tau_2}, \dots, p_{\tau_d})$.
 157 Similar to the above-described notations, we can replace the index i in $[\mathbf{K}_i]_i$ and
 158 $\text{diag}_i(\mathbf{K}_i)$ with an index set τ , a multi-index \mathbf{c} , or a multi-set $\boldsymbol{\tau}$ assuming certain
 159 predefined index ordering.

160 Given complex-valued (or real-valued) functions $f(x)$ of d variables and inte-
 161 gral operators $K(x, y)$, the tensor representations of their discretizations are respec-
 162 tively denoted by $\mathcal{F} \in \mathbb{C}^{n_1 \times n_2 \times \dots \times n_d}$ and $\mathcal{K} \in \mathbb{C}^{m_1 \times m_2 \times \dots \times m_d \times n_1 \times n_2 \times \dots \times n_d}$, where
 163 n_1, \dots, n_d and m_1, \dots, m_d are sizes of discretizations for the corresponding vari-
 164 ables. In this paper, we use *matricization* to denote the reshaping of \mathcal{K} into a
 165 $(\prod_k m_k) \times (\prod_k n_k)$ matrix, and the reshaping of \mathcal{F} into a $(\prod_k n_k) \times 1$ matrix. The entries
 166 of \mathcal{F} and \mathcal{K} are denoted by $\mathcal{F}(\mathbf{i})$ (or equivalently $\mathcal{F}(i_1, i_2, \dots, i_d)$) and $\mathcal{K}(\mathbf{i}, \mathbf{j})$, respec-
 167 tively. Similarly the subtensors are denoted by $\mathcal{F}(\boldsymbol{\tau})$ (or equivalently $\mathcal{F}(\tau_1, \tau_2, \dots, \tau_d)$)
 168 and $\mathcal{K}(\boldsymbol{\tau}, \boldsymbol{\nu})$.

169 Given a d -mode tensor $\mathcal{F} \in \mathbb{C}^{n_1 \times n_2 \times \dots \times n_d}$, the mode- j unfolding is denoted by
 170 $\mathbf{F}^{(j)} \in \mathbb{C}^{(\prod_{k \neq j} n_k) \times n_j}$, the mode- j tensor-matrix product of \mathcal{F} with a matrix $\mathbf{X} \in$
 171 $\mathbb{C}^{m \times n_j}$ is denoted by $\mathcal{Y} = \mathcal{F} \times_j \mathbf{X}$, or equivalently $\mathbf{Y}^{(j)} = \mathbf{F}^{(j)} \mathbf{X}^T$.

172 **2. Review of Matrix Algorithms.** We consider a d -dimensional OIO kernel
 173 $K(x, y)$ with $x, y \in \mathbb{R}^d$ discretized on point pairs x^i and y^j , $i = 1, 2, \dots, (m_1 m_2 \cdot$
 174 $\dots m_d)$, $j = 1, 2, \dots, (n_1 n_2 \cdot \dots n_d)$, where i (and similarly j) is the flattening of the
 175 corresponding multi-index \mathbf{i} . Such a discretization can be represented as a matrix
 176 $\mathbf{K} \in \mathbb{C}^{(m_1 m_2 \dots m_d) \times (n_1 n_2 \dots n_d)}$. When it is clear in the context, we assume that $m_k =$
 177 $n_k = n$ for $k = 1, \dots, d$. Throughout this paper, we assume that \mathbf{K} (and its tensor
 178 representation) is never fully formed, but instead a function is provided to evaluate any
 179 matrix (or tensor) entry in $O(1)$ time. Next we review matrix compression algorithms
 180 for \mathbf{K} including low-rank and butterfly algorithms.

181 **2.1. Interpolative Decomposition.** The interpolative decomposition (ID) al-
 182 gorithm [29, 39] is a matrix compression technique that constructs a low-rank de-
 183 composition whose factors contain original entries of the matrix. More specifically,
 184 consider the matrix $\mathbf{K}(\tau, \nu) \in \mathbb{C}^{m \times n}$, $\tau = \{1, 2, \dots, m\}$, $\nu = \{1, 2, \dots, n\}$, the column
 185 ID of \mathbf{K} (the index sets τ and ν are omitted for clarity in context) is

$$186 \quad (2.1) \quad \mathbf{K} \approx \mathbf{K}(:, \bar{\nu})\mathbf{V},$$

187 where the skeleton matrix $\mathbf{K}(:, \bar{\nu})$ contains r skeleton columns indexed by $\bar{\nu} \subseteq \nu$ and
 188 the interpolation matrix \mathbf{V} has bounded entries. Here the numerical rank r is chosen
 189 such that

$$190 \quad (2.2) \quad \|\mathbf{K} - \mathbf{K}(:, \bar{\nu})\mathbf{V}\|_F^2 \leq O(\epsilon^2)\|\mathbf{K}\|_F^2$$

191 for a prescribed relative tolerance ϵ . In practice, the column ID can be computed via
 192 rank-revealing QR decomposition with a relative tolerance ϵ [39]. Similarly, the row
 193 ID of the matrix \mathbf{K} reads

$$194 \quad (2.3) \quad \mathbf{K} \approx \mathbf{U}\mathbf{K}(\bar{\tau}, :),$$

195 where the skeleton matrix $\mathbf{K}(\bar{\tau}, :)$ contains r skeleton rows indexed by $\bar{\tau} \subseteq \tau$ and the
 196 interpolation matrix \mathbf{U} has bounded entries. The row ID can be simply computed by
 197 the column ID of \mathbf{K}^T . Combining the column and row ID in (2.1) and (2.3) gives

$$198 \quad (2.4) \quad \mathbf{K} \approx \mathbf{U}\mathbf{K}(\bar{\tau}, \bar{\nu})\mathbf{V}.$$

199 It is straightforward to note that the memory and CPU complexities of ID scale as
 200 $O(nr)$ and $O(n^2r)$, respectively. The CPU complexity can be reduced to $O(nr^2)$
 201 when properly selected proxy rows in (2.1) and columns in (2.3) are used in the rank-
 202 revealing QR. Common strategies of choosing proxy rows/columns (henceforth called
 203 *proxy index* strategies) for integral operators include evenly spaced or uniform random
 204 samples, and more generally the use of Chebyshev nodes and proxy surfaces (where
 205 new rows $K(\bar{x}, y^j)$ other than original rows of \mathbf{K} are used with \bar{x} denoting the proxies).
 206 However, for large OIOs (e.g., Green's functions of high-frequency wave equations
 207 discretized with a small number of points per wavelength), the rank r depends on the
 208 size n of the matrix; consequently, ID is not an efficient compression algorithm. Next,
 209 we review the matrix butterfly algorithm capable of achieving quasi-linear memory
 210 and CPU complexities for OIOs.

211 **2.2. Matrix Butterfly Algorithm.** For reasons discussed in subsection 1.1,
 212 we only consider the binary tree based matrix butterfly algorithm as the reference
 213 algorithm for the proposed tensor butterfly algorithm throughout this paper. Let
 214 $t^0 = \{1, 2, \dots, m\}$ and $s^0 = \{1, 2, \dots, n\}$. Without loss of generality, we assume that
 215 $m = n$. The L -level butterfly representation of the discretized OIO $\mathbf{K}(t^0, s^0)$ is based
 216 on two binary trees, \mathcal{T}_{t^0} and \mathcal{T}_{s^0} , and the CLR property of the OIO takes the following
 217 form: at any level $0 \leq l \leq L$, for any node τ at level l of \mathcal{T}_{t^0} and any node ν at level
 218 $L - l$ of \mathcal{T}_{s^0} , the subblock $\mathbf{K}(\tau, \nu)$ is numerically low-rank with rank $r_{\tau, \nu}$ bounded by
 219 a small number r called the butterfly rank [47, 36, 37, 58].

220 For any subblock $\mathbf{K}(\tau, \nu)$, the ID in (2.4) permits

$$221 \quad (2.5) \quad \mathbf{K}(\tau, \nu) \approx \mathbf{U}_{\tau, \nu}\mathbf{K}(\bar{\tau}, \bar{\nu})\mathbf{V}_{\tau, \nu},$$

222 where the skeleton rows and columns are indexed by $\bar{\tau}$ and $\bar{\nu}$, respectively. It is worth
 223 noting that given a node ν , the selection of skeleton columns $\bar{\nu}$ depends on the node

224 τ . However, the notation $\bar{\cdot}$ does not reflect the dependency when it is clear in the
 225 context. By CLR, there are at most r skeleton rows and columns.

226 Without loss of generality, we assume that L is an even number so that $L^c = L/2$
 227 denotes the middle level. At levels $l = 0, \dots, L^c$, the interpolation matrices $\mathbf{V}_{\tau, \nu}$ are
 228 computed as follows:

229 At level $l = 0$, $\mathbf{V}_{\tau, \nu}$ are explicitly formed. While at level $0 < l \leq L^c$, they are
 230 represented in a nested fashion. To see this, consider a node pair (τ, ν) at level $l > 0$
 231 and let ν^1, ν^2 and p_τ be the children and parent of ν and τ , respectively. Let s be the
 232 ancestor of ν at level L^c of \mathcal{T}_{s^0} and let \mathcal{T}_s denote the subtree rooted at s .

233 By (2.4), we have

$$\begin{aligned} 234 \quad \mathbf{K}(\tau, \nu) &= [\mathbf{K}(\tau, \nu^1) \quad \mathbf{K}(\tau, \nu^2)] \\ 235 \quad (2.6) \quad &\approx [\mathbf{K}(\tau, \bar{\nu}^1) \quad \mathbf{K}(\tau, \bar{\nu}^2)] \begin{bmatrix} \mathbf{V}_{p_\tau, \nu^1}^s & \\ & \mathbf{V}_{p_\tau, \nu^2}^s \end{bmatrix} \\ 236 \quad (2.7) \quad &\approx \mathbf{K}(\tau, \bar{\nu}) \mathbf{W}_{\tau, \nu}^s \begin{bmatrix} \mathbf{V}_{p_\tau, \nu^1}^s & \\ & \mathbf{V}_{p_\tau, \nu^2}^s \end{bmatrix}. \\ 237 \end{aligned}$$

238 Here $\mathbf{W}_{\tau, \nu}^s$ and $\bar{\nu}$ are the interpolation matrix and skeleton columns from the ID of
 239 $\mathbf{K}(\tau, \bar{\nu}^1 \cup \bar{\nu}^2)$, respectively. $\mathbf{W}_{\tau, \nu}$ is henceforth referred to as the transfer matrix for
 240 ν in the rest of this paper. By CLR, $\mathbf{W}_{\tau, \nu}$ is of sizes at most $r \times 2r$. Note that we
 241 have added an additional superscript s to $\mathbf{V}_{p_\tau, \nu^c}$ and $\mathbf{W}_{\tau, \nu}$, for notation convenience
 242 in the later context. From (2.6), it is clear that the interpolation matrix $\mathbf{V}_{\tau, \nu}^s$ can be
 243 expressed in terms of its parent p_τ 's and children ν^1, ν^2 's interpolation matrices as

$$244 \quad (2.8) \quad \mathbf{V}_{\tau, \nu}^s = \mathbf{W}_{\tau, \nu}^s \begin{bmatrix} \mathbf{V}_{p_\tau, \nu^1}^s & \\ & \mathbf{V}_{p_\tau, \nu^2}^s \end{bmatrix}.$$

245 Note that the interpolation matrices $\mathbf{V}_{\tau, \nu}^s$ at level $l = 0$ and transfer matrices $\mathbf{W}_{\tau, \nu}^s$
 246 at level $0 < l \leq L^c$ do not require the column ID on the full subblocks $\mathbf{K}(\tau, \nu)$ and
 247 $\mathbf{K}(\tau, \bar{\nu}^1 \cup \bar{\nu}^2)$, which would lead to at least an $O(mn)$ computational complexity.

248 In practice, one can select $O(r_{\tau, \nu})$ proxy rows $\hat{\tau} \subset \tau$ to compute $\mathbf{V}_{\tau, \nu}^s$ and $\mathbf{W}_{\tau, \nu}^s$
 249 via ID as:

$$250 \quad (2.9) \quad \mathbf{K}(\hat{\tau}, \nu) \approx \mathbf{K}(\hat{\tau}, \bar{\nu}) \mathbf{V}_{\tau, \nu}^s, \quad l = 0,$$

$$251 \quad (2.10) \quad \mathbf{K}(\hat{\tau}, \bar{\nu}^1 \cup \bar{\nu}^2) \approx \mathbf{K}(\hat{\tau}, \bar{\nu}) \mathbf{W}_{\tau, \nu}^s, \quad 0 < l \leq L^c.$$

253 The viable choices for proxy rows have been discussed in several existing papers [45,
 254 58, 61, 8].

255 At levels $l = L^c, \dots, L$, the interpolation matrices $\mathbf{U}_{\tau, \nu}$ are computed by perform-
 256 ing similar operations on \mathbf{K}^T . We only provide their expressions here and omit the
 257 redundant explanation. Let t be the ancestor of ν at level L^c of \mathcal{T}_{t^0} and let \mathcal{T}_t be the
 258 subtree rooted at t . At level $l = L$, $\mathbf{U}_{\tau, \nu}^t$ are explicitly formed. At level $L^c \leq l < L$,
 259 only the transfer matrices $\mathbf{P}_{\tau, \nu}^t$ are computed from the column ID of $\mathbf{K}^T(\nu, \bar{\tau}^1 \cup \bar{\tau}^2)$
 260 satisfying

$$261 \quad (2.11) \quad \mathbf{U}_{\tau, \nu}^t = \begin{bmatrix} \mathbf{U}_{\tau^1, p_\nu}^t & \\ & \mathbf{U}_{\tau^2, p_\nu}^t \end{bmatrix} \mathbf{P}_{\tau, \nu}^t.$$

262 Combining (2.5), (2.8) and (2.11), the matrix butterfly decomposition can be

Meaning	Matrix butterfly	Tensor butterfly
Butterfly rank	r_m	r_t
Set/multi-set	τ, ν	$\boldsymbol{\tau}, \boldsymbol{\nu}$
k^{th} set of multi-set	-	τ_k, ν_k
Parent set/multi-set	p_τ	\boldsymbol{p}_τ
Children set/multi-set	τ^c	$\boldsymbol{\tau}^c$
Root-level set/multi-set	t^0, s^0	$\boldsymbol{t}^0, \boldsymbol{s}^0$
Mid-level set/multi-set	t, s	$\boldsymbol{t}, \boldsymbol{s}$
Binary tree	$\mathcal{T}_{t^0}, \mathcal{T}_{s^0}$	$\mathcal{T}_{t_k^0}, \mathcal{T}_{s_k^0}$
Cardinality of leaf nodes	C_b^d	C_b
Cardinality of root nodes	n^d	n
Mid-level submatrix/subtensor	$\mathbf{K}(\bar{t}, \bar{s})$	$\boldsymbol{\mathcal{K}}(\bar{\boldsymbol{t}}, \bar{\boldsymbol{s}})$
Interpolation matrix	$\mathbf{V}_{\tau, \nu}^s, \mathbf{U}_{\tau, \nu}^t$	$\mathbf{V}_{\tau, \nu}^{s, k}, \mathbf{U}_{\tau, \nu}^{t, k}$
Transfer matrix	$\mathbf{W}_{\tau, \nu}^s, \mathbf{P}_{\tau, \nu}^t$	$\mathbf{W}_{\tau, \nu}^{s, k}, \mathbf{P}_{\tau, \nu}^{t, k}$
Interpolation factor	$\bar{\mathbf{U}}^t, \bar{\mathbf{V}}^s$	$\bar{\mathbf{U}}^{t, k}, \bar{\mathbf{V}}^{s, k}$
Transfer factor	$\bar{\mathbf{P}}_l^{t, s}, \bar{\mathbf{W}}_l^{t, s}$	$\bar{\mathbf{P}}_l^{t, s, k}, \bar{\mathbf{W}}_l^{t, s, k}$

Table 2.1: Notation comparison of the matrix butterfly algorithm in [subsection 2.2](#) and the tensor butterfly algorithm in [subsection 3.2](#). Note that the subscript k in τ_k, ν_k , in the tensor notations of the interpolation/transfer matrix and interpolation/transfer factor for dimension k , is dropped for simplicity throughout this paper.

263 expressed for each node pair (t, s) at level L^c of \mathcal{T}_{t^0} and \mathcal{T}_{s^0} as

264 (2.12)
$$\mathbf{K}(t, s) \approx \bar{\mathbf{U}}^t \left(\prod_{l=1}^{L^c} \bar{\mathbf{P}}_l^{t, s} \right) \mathbf{K}(\bar{t}, \bar{s}) \left(\prod_{l=L^c}^1 \bar{\mathbf{W}}_l^{t, s} \right) \bar{\mathbf{V}}^s.$$

265

266 Here, \bar{t} and \bar{s} represent the skeleton rows and columns of the ID of $\mathbf{K}(t, s)$. The
267 interpolation factors $\bar{\mathbf{U}}^t$ and $\bar{\mathbf{V}}^s$ in (2.12) are

268 (2.13)
$$\bar{\mathbf{U}}^t = \text{diag}_\tau(\mathbf{U}_{\tau, s^0}^t), \quad \tau \text{ at level } L^c \text{ of } \mathcal{T}_t,$$

269 (2.14)
$$\bar{\mathbf{V}}^s = \text{diag}_\nu(\mathbf{V}_{t^0, \nu}^s), \quad \nu \text{ at level } L^c \text{ of } \mathcal{T}_s,$$

271 and the transfer factors $\bar{\mathbf{P}}_l^{t, s}$ and $\bar{\mathbf{W}}_l^{t, s}$ for $l = 1, \dots, L^c$ consist of transfer matrices
272 $\mathbf{W}_{\tau, \nu}^s$ and $\mathbf{P}_{\tau, \nu}^s$:

273 (2.15)
$$\bar{\mathbf{W}}_l^{t, s} = \text{diag}_\tau \left(\left[\text{diag}_\nu(\mathbf{W}_{\tau^c, \nu}^s) \right]_c \right), \quad \begin{array}{l} \tau \text{ at level } l-1 \text{ of } \mathcal{T}_{t^0}, \text{ and } t \subseteq \tau, \\ \nu \text{ at level } L^c - l \text{ of } \mathcal{T}_s; \end{array}$$

274 (2.16)
$$(\bar{\mathbf{P}}_l^{t, s})^T = \text{diag}_\nu \left(\left[\text{diag}_\tau((\mathbf{P}_{\tau, \nu^c}^t)^T) \right]_c \right), \quad \begin{array}{l} \tau \text{ at level } L^c - l \text{ of } \mathcal{T}_t, \\ \nu \text{ at level } l-1 \text{ of } \mathcal{T}_{s^0}, \text{ and } s \subseteq \nu. \end{array}$$

275

276 Here τ^c and ν^c with $c = 1, 2$ are children of τ and ν , respectively. For the ease
277 of comparison with the tensor butterfly algorithm in [subsection 3.2](#), we list some
278 notations of the matrix butterfly algorithm in [Table 2.1](#).

279 The CPU and memory requirement for computing the matrix butterfly decom-
280 position can be briefly analyzed as follows. Note that we only need to analyze the

281 costs for $\mathbf{V}_{\tau,\nu}^s$, $\mathbf{W}_{\tau,\nu}^s$ and $\mathbf{K}(\bar{t}, \bar{s})$ as those for $\mathbf{U}_{\tau,\nu}^t$ and $\mathbf{P}_{\tau,\nu}^t$ are similar. By the CLR
 282 assumption, we assume that $r_{\tau,\nu} \leq r, \forall \tau, \nu$ for some constant r . Thanks to the use
 283 of the proxy rows and columns, the computation of one individual $\mathbf{V}_{\tau,\nu}^s$ and $\mathbf{W}_{\tau,\nu}^s$ by
 284 ID only operates on $O(r) \times O(r)$ matrices, hence its memory and CPU requirements
 285 are $O(r^2)$ and $O(r^3)$, respectively. In total, there are $O(2^{L^c})$ middle-level nodes s
 286 each having $O(2^{L^c})$ numbers of $\mathbf{V}_{\tau,\nu}^s$ and $O(L^c 2^{L^c})$ numbers of $\mathbf{W}_{\tau,\nu}^s$. Similarly, each
 287 $\mathbf{K}(\bar{t}, \bar{s})$ requires $O(r^2)$ CPU and memory costs, and there are in total $O(2^L)$ middle-
 288 level node pairs (t, s) . These numbers sum up to the overall $O(nr^2 \log n)$ memory and
 289 $O(nr^3 \log n)$ CPU complexities for matrix butterfly algorithms.

290 For d -dimensional discretized OIOs $\mathbf{K} \in \mathbb{C}^{(m_1 m_2 \dots m_d) \times (n_1 n_2 \dots n_d)}$ with $m_k = n_k =$
 291 n , we can assume that $n = C_b 2^L$ with some constant C_b . For the above-described
 292 binary-tree-based butterfly algorithm, the leaf nodes of the trees are of size C_b^d and
 293 this leads to a dL -level butterfly factorization. The memory and CPU complexities for
 294 this algorithm become $O(dn^d r^2 \log n)$ and $O(dn^d r^3 \log n)$, respectively. On the other
 295 hand, the multi-dimensional tree-based butterfly algorithm [38, 10] leads to a L -level
 296 factorization with $O(2^d n^d r^2 \log n)$ memory and $O(2^d n^d r^3 \log n)$ CPU complexities.
 297 In this paper, we only use the binary-tree-based algorithm as the baseline matrix
 298 butterfly algorithm. Despite their quasi-linear complexity for high-dimensional OIOs,
 299 the butterfly rank r is constant but high, leading to very large prefactors of these
 300 binary and multi-dimensional tree-based algorithms. In the following, we turn to tensor
 301 decomposition algorithms to reduce both the prefactor and asymptotic scaling of
 302 matrix butterfly algorithms. The proposed tensor decomposition explores additional
 303 tensor compressibility of high-dimensional OIOs such as translational invariance of
 304 free-space Green's functions and dimensional separability of Fourier transforms. As
 305 will be clear in the next section, the prefactor (dependent on the butterfly rank) can
 306 be reduced by leveraging Tucker decomposition for tensorization of the middle-level
 307 submatrices $\mathbf{K}(\bar{t}, \bar{s})$ of (2.12). The Tucker decomposition is further factored out along
 308 each dimension in a nested fashion by simultaneously moving along the binary tree
 309 of that dimension and d binary trees of other dimensions. As a result, the number
 310 of transfer matrices becomes dominant only towards the middle level L^c , leading to a
 311 factor of $\log n$ reduction in the asymptotic complexity.

312 **3. Proposed Tensor Algorithms.** In this section, we assume that the d -
 313 dimensional discretized OIO in section 2 is directly represented as a $2d$ -mode tensor
 314 $\mathcal{K} \in \mathbb{C}^{m_1 \times m_2 \times \dots \times m_d \times n_1 \times n_2 \times \dots \times n_d}$. We first extend the matrix ID algorithm in sub-
 315 section 2.1 to its tensor variant, which serves as the building block for the proposed
 316 tensor butterfly algorithm.

317 **3.1. Tucker-type Interpolative Decomposition.** Given the $2d$ -mode tensor
 318 $\mathcal{K}(\tau, \nu)$ with $\tau_k = \{1, 2, \dots, m_k\}$ and $\nu_k = \{1, 2, \dots, n_k\}$ for $k = 1, \dots, d$, the pro-
 319 posed Tucker-type decomposition compresses each dimension independently via the
 320 column ID of the unfolding of \mathcal{K} along the k -th dimension,

$$321 \quad (3.1) \quad \mathbf{K}^{(k)} \approx \mathbf{K}^{(k)}(:, \overline{\tau_k}) \mathbf{U}^k, \quad \mathbf{K}^{(d+k)} \approx \mathbf{K}^{(d+k)}(:, \overline{\nu_k}) \mathbf{V}^k, \quad k = 1, \dots, d,$$

322 where $\mathbf{K}^{(k)} \in \mathbb{C}^{(\prod_{j \neq k} n_j) \times n_k}$ is the mode- k unfolding, or equivalently

$$323 \quad (3.2) \quad \mathcal{K} \approx \mathcal{K}(\tau_{k \leftarrow \overline{\tau_k}}, \nu) \times_k \mathbf{U}^k, \quad \mathcal{K} \approx \mathcal{K}(\tau, \nu_{k \leftarrow \overline{\nu_k}}) \times_{d+k} \mathbf{V}^k, \quad k = 1, \dots, d.$$

324 Here, $\overline{\tau_k}$ and $\overline{\nu_k}$ denote the skeleton indices along modes k and $d+k$ of \mathcal{K} , respectively,
 325 while $\tau_{k \leftarrow \overline{\tau_k}}$ and $\nu_{k \leftarrow \overline{\nu_k}}$ denote multi-sets that replace τ_k and ν_k , respectively, with $\overline{\tau_k}$

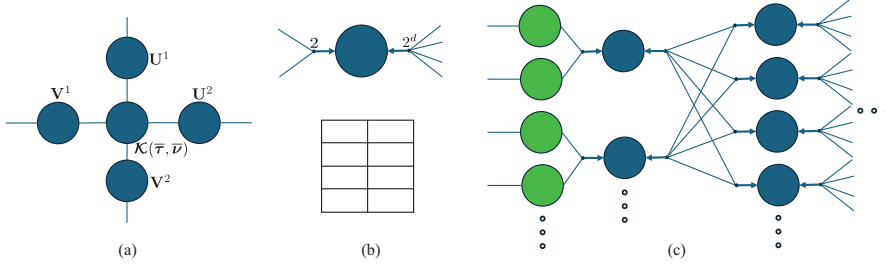


Fig. 3.1: Tensor diagrams for (a) the Tucker-ID decomposition of a 4-mode tensor, and (b) the matrix partitioner corresponding to a $2^d \times 2$ partitioning with $d = 2$ used in the tensor butterfly decomposition of a $2d$ -mode tensor, such as $\left[\mathbf{W}_{\tau^c, \nu}^{s, k} \right]_{\mathbf{c}}$ in (3.14) for fixed \mathbf{s}, τ, k and ν , or $\left[\mathbf{P}_{\tau, \nu^c}^{t, k} \right]_{\mathbf{c}}$ in (3.13) for fixed \mathbf{t}, ν, k and τ . Here, each of the row and column dimensions is connected to a partitioning node. Each partitioning node has a parent edge with an arrow pointing to the dimension to be partitioned, and several children edges connected to the parent edge. The weight of the parent edge (i.e., the number of columns or rows of the matrix) equals the sum of the weights of the children edges. (c) The tensor diagram involving blocks $\mathbf{V}_{\mathbf{t}^0, \nu}^{s, k}$ (in green) and blocks $\left[\mathbf{W}_{\tau^c, \nu}^{s, k} \right]_{\mathbf{c}}$ (in blue) for fixed \mathbf{s} and k for the tensor butterfly decomposition of a $2d$ -mode tensor.

326 and $\bar{\nu}_k$. Combining (3.2) for all dimensions yields the following proposed Tucker-type
 327 decomposition,

328 (3.3)
$$\mathcal{K} \approx \mathcal{K}(\bar{\tau}, \bar{\nu}) \left(\prod_{k=1}^d \times_k \mathbf{U}^k \right) \left(\prod_{k=1}^d \times_{d+k} \mathbf{V}^k \right),$$

329 where, $\bar{\tau} = (\bar{\tau}_1, \bar{\tau}_2, \dots, \bar{\tau}_d)$, $\bar{\nu} = (\bar{\nu}_1, \bar{\nu}_2, \dots, \bar{\nu}_d)$, the core tensor $\mathcal{K}(\bar{\tau}, \bar{\nu})$ is a subtensor
 330 of \mathcal{K} , and \mathbf{U}^k and \mathbf{V}^k are the factor matrices for modes k and $d+k$, respectively.

331 See Figure 3.1(a) for the tensor diagram of (3.3) for a 4-mode tensor, which
 332 has the same diagram as other existing Tucker decompositions such as high-order
 333 singular value decompositions (HOSVD) [16]. However, unlike HOSVD that leads to
 334 orthonormal factor matrices, the proposed decomposition leads to factor matrices with
 335 bounded entries and the core tensor with the original tensor entries. Therefore, the
 336 proposed decomposition is named Tucker-type interpolative decomposition (Tucker-
 337 ID). It is worth noting that there exist several interpolative tensor decomposition
 338 algorithms [6, 51, 52, 60, 55]. However they either use original tensor entries in the
 339 factor matrices (instead of the core tensor) [51, 60, 6] or rely on a different tensor
 340 diagram [52]. Note that the structure-preserving decomposition in [55] is similar to
 341 Tucker-ID but relies on sketching instead of proxy indices for the construction. As will
 342 be seen in subsection 3.2, the Tucker-ID algorithm is a unique and essential building
 343 block of the tensor butterfly algorithm.

344 Just like HOSVD, one can easily show that if the approximations in (3.1) hold
 345 true up to a predefined relative compression tolerance ϵ as

346 (3.4)
$$\begin{aligned} \|\mathbf{K}^{(k)} - \mathbf{K}^{(k)}(:, \bar{\tau}_k) \mathbf{U}^k\|_F &\leq \epsilon \|\mathcal{K}\|_F, \quad k = 1, \dots, d, \\ \|\mathbf{K}^{(d+k)} - \mathbf{K}^{(d+k)}(:, \bar{\nu}_k) \mathbf{V}^k\|_F &\leq \epsilon \|\mathcal{K}\|_F, \quad k = 1, \dots, d, \end{aligned}$$

349 then the Tucker-ID of (3.3) satisfies

$$350 \quad (3.5) \quad \left\| \mathcal{K} - \mathcal{K}(\bar{\tau}, \bar{\nu}) \left(\prod_{k=1}^d \times_k \mathbf{U}^k \right) \left(\prod_{k=1}^d \times_{d+k} \mathbf{V}^k \right) \right\|_F \leq \epsilon \sqrt{2d} \|\mathcal{K}\|_F.$$

351

352 The memory and CPU complexities of Tucker-ID can be briefly analyzed as fol-
 353 lows. Assuming that $m_k = n_k = n$ and $\max_k |\bar{\tau}_k| = \max_k |\bar{\nu}_k| = r$ is a constant (we
 354 will discuss the case of non-constant r in subsection 3.2.3), the memory requirement
 355 is simply $O(drn + r^{2d})$, where the first and second term represent the storage units
 356 for the factor matrices and the core tensor, respectively. The CPU cost for naive
 357 computation of Tucker-ID is $O(drn^{2d} + r^{2d})$, where the first term represents the cost
 358 of rank-revealing QR of the unfolding matrices in (3.1), and the second term repre-
 359 sents the cost forming the core tensor $\mathcal{K}(\bar{\tau}, \bar{\nu})$. In practice, however, the unfolding
 360 matrices do not need to be fully formed and one can leverage the idea of proxy rows
 361 in subsection 2.2 to reduce the cost for computing the factor matrices to $O(dnr^{2d})$.
 362 We will explain this in more detail in the context of the proposed tensor butterfly
 363 decomposition algorithm.

364 Just like the matrix ID algorithm, Tucker-ID is also not suitable for representing
 365 large-sized OIOs as the rank r depends on the size n . That said, the Tucker-ID rank
 366 is typically significantly smaller than the matrix ID rank, as it exploits more com-
 367 pressibility properties across dimensions by leveraging e.g. translational-invariance
 368 or dimensional-separability properties of OIOs; see subsection 3.2.1 for a few of such
 369 examples. In what follows, we use Tucker-ID as the building block for constructing a
 370 linear-complexity tensor butterfly decomposition algorithm for large-sized OIOs.

371 **3.2. Tensor Butterfly Algorithm.** Consider a 2d-mode OIO tensor $\mathcal{K}(\mathbf{t}^0, \mathbf{s}^0)$
 372 with $\mathbf{t}^0 = (t_1^0, t_1^0, \dots, t_d^0)$, $\mathbf{s}^0 = (s_1^0, s_1^0, \dots, s_d^0)$, $t_k^0 = \{1, 2, \dots, m_k\}$, $s_k^0 = \{1, 2, \dots, n_k\}$,
 373 $k = 1, 2, \dots, d$. Without loss of generality, we assume that $m_k = n_k = n$. We further
 374 assume that each t_k^0 (and s_k^0) is binary partitioned with a tree $\mathcal{T}_{t_k^0}$ (and $\mathcal{T}_{s_k^0}$) of L levels
 375 for $k = 1, 2, \dots, d$.

376 To start with, we first define the tensor CLR property as follows:

- 377 • For any level $0 \leq l \leq L^c$, any multi-set $\boldsymbol{\tau} = (\tau_1, \tau_2, \dots, \tau_d)$ with $\tau_i, i \leq d$ at level
 378 l of $\mathcal{T}_{t_i^0}$, any multi-set $\mathbf{s} = (s_1, s_2, \dots, s_d)$ with $s_i, i \leq d$ at level L^c of $\mathcal{T}_{s_i^0}$, any
 379 mode $1 \leq k \leq d$, and any node ν at level $L^c - l$ of \mathcal{T}_{s_k} , the mode- $(d+k)$ unfolding
 380 of the subtensor $\mathcal{K}(\boldsymbol{\tau}, \mathbf{s}_{k \leftarrow \nu})$ is numerically low-rank (with rank bounded by r),
 381 permitting an ID via (3.2):

$$382 \quad (3.6) \quad \mathcal{K}(\boldsymbol{\tau}, \mathbf{s}_{k \leftarrow \nu}) \approx \mathcal{K}(\boldsymbol{\tau}, \mathbf{s}_{k \leftarrow \bar{\nu}}) \times_{d+k} \mathbf{V}_{\boldsymbol{\tau}, \nu}^{\mathbf{s}, k}.$$

- 383 • For any level $0 \leq l \leq L^c$, any multi-set $\boldsymbol{\nu} = (\nu_1, \nu_2, \dots, \nu_d)$ with $\nu_i, i \leq d$ at level
 384 l of $\mathcal{T}_{s_i^0}$, any multi-set $\mathbf{t} = (t_1, t_2, \dots, t_d)$ with $t_i, i \leq d$ at level L^c of $\mathcal{T}_{t_i^0}$, any
 385 mode $1 \leq k \leq d$, and any node τ at level $L^c - l$ of \mathcal{T}_{t_k} , the mode- k unfolding of the
 386 subtensor $\mathcal{K}(\mathbf{t}_{k \leftarrow \tau}, \boldsymbol{\nu})$ is numerically low-rank (with rank bounded by r), permitting
 387 an ID via (3.2):

$$388 \quad (3.7) \quad \mathcal{K}(\mathbf{t}_{k \leftarrow \tau}, \boldsymbol{\nu}) \approx \mathcal{K}(\mathbf{t}_{k \leftarrow \bar{\tau}}, \boldsymbol{\nu}) \times_k \mathbf{U}_{\boldsymbol{\tau}, \nu}^{\mathbf{t}, k}.$$

389 In essence, the tensor CLR in (3.6) and (3.7) investigates the unfolding of judiciously
 390 selected subtensors rather than the matricization used in the matrix CLR. Moreover,
 391 the tensor CLR requires fixing $d - 1$ modes of the 2d-mode subtensors to be of size
 392 $O(\sqrt{n})$ while changing the remaining $d + 1$ modes with respect to l . Therefore each

393 ID computation can operate on larger subtensors compared to the matrix CLR. In
 394 [subsection 3.2.1](#) we provide two examples, namely a free-space Green's function tensor
 395 and a high-dimensional Fourier transform, to explain why the tensor CLR is valid, and
 396 in [subsection 3.2.2](#) we will see that the tensor CLR essentially reduces the quasilinear
 397 complexity of the matrix butterfly algorithm to linear complexity. Here, assuming
 398 that the tensor CLR holds true, we describe the tensor butterfly algorithm. We note
 399 that there may be alternative ways to define the tensor CLR different from (3.6) and
 400 (3.7), and we leave that as a future work. To avoid notation confusion, we list some
 401 notations of the tensor butterfly algorithm in [Table 2.1](#).

402 In what follows, we focus on the computation of $\mathbf{V}_{\tau,\nu}^{s,k}$ (corresponding to the
 403 mid-level multi-set \mathbf{s}), as $\mathbf{U}_{\tau,\nu}^{t,k}$ (corresponding to the mid-level multi-set \mathbf{t}) can be
 404 computed in a similar fashion. At level $l = 0$, $\mathbf{V}_{\tau,\nu}^{s,k}$ are explicitly formed. At level
 405 $0 < l \leq L^c$, they are represented in a nested fashion. Let $\mathbf{p}_\tau = (p_{\tau_1}, p_{\tau_2}, \dots, p_{\tau_d})$
 406 consist of parents of $\tau = (\tau_1, \tau_2, \dots, \tau_d)$ in (3.6).

407 By the tensor CLR property, we have

$$\begin{aligned}
 408 \quad \mathcal{K}(\tau, \mathbf{s}_{k \leftarrow \nu}) &\approx \mathcal{K}(\tau, \mathbf{s}_{k \leftarrow \overline{\nu^1 \cup \nu^2}}) \times_{d+k} \begin{bmatrix} \mathbf{V}_{\mathbf{p}_\tau, \nu^1}^{s,k} & \\ & \mathbf{V}_{\mathbf{p}_\tau, \nu^2}^{s,k} \end{bmatrix} \\
 409 \quad (3.8) \quad &\approx \mathcal{K}(\tau, \mathbf{s}_{k \leftarrow \overline{\nu}}) \times_{d+k} \left(\mathbf{W}_{\tau,\nu}^{s,k} \begin{bmatrix} \mathbf{V}_{\mathbf{p}_\tau, \nu^1}^{s,k} & \\ & \mathbf{V}_{\mathbf{p}_\tau, \nu^2}^{s,k} \end{bmatrix} \right). \\
 410
 \end{aligned}$$

411 Comparing (3.8) and (3.6), one realizes that the interpolation matrix $\mathbf{V}_{\tau,\nu}^{s,k}$ is
 412 represented as the product of the transfer matrix $\mathbf{W}_{\tau,\nu}^{s,k}$ and $\text{diag}_{\mathbb{S}^c}(\mathbf{V}_{\mathbf{p}_\tau, \nu^c}^{s,k})$. Here, the
 413 transfer matrix $\mathbf{W}_{\tau,\nu}^{s,k}$ is computed as the interpolation matrix of the column ID of
 414 the mode- $(d+k)$ unfolding of $\mathcal{K}(\tau, \mathbf{s}_{k \leftarrow \overline{\nu^1 \cup \nu^2}})$. As mentioned in [section 3](#), in practice
 415 one never forms the unfolding matrix in full, but instead considers the unfolding of
 416 $\mathcal{K}(\hat{\tau}, \hat{\mathbf{s}}_{k \leftarrow \overline{\nu^1 \cup \nu^2}})$, where $\hat{\tau} = (\hat{\tau}_1, \hat{\tau}_2, \dots, \hat{\tau}_d)$ and $\hat{\mathbf{s}} = (\hat{s}_1, \hat{s}_2, \dots, \hat{s}_d)$; here $\hat{\tau}_i$ and \hat{s}_i
 417 consist of $O(r)$ judiciously selected indices along modes i and $d+i$, respectively. Note
 418 that \hat{s}_k is never used as it is replaced by $\overline{\nu^1 \cup \nu^2}$ in (3.8). The same proxy index
 419 strategy can be used to obtain $\mathbf{V}_{\tau,\nu}^{s,k}$ at the level $l = 0$. For each $\mathbf{W}_{\tau,\nu}^{s,k}$ or $\mathbf{V}_{\tau,\nu}^{s,k}$, its
 420 computation requires $O(r^{2d+1})$ CPU time.

421 Similarly in (3.7), $\mathbf{U}_{\tau,\nu}^{t,k}$ is explicitly formed at $l = 0$ and constructed via the
 422 transfer matrix $\mathbf{P}_{\tau,\nu}^{t,k}$ at level $0 < l \leq L^c$:

$$\begin{aligned}
 423 \quad \mathcal{K}(\mathbf{t}_{k \leftarrow \tau}, \nu) &\approx \mathcal{K}(\mathbf{t}_{k \leftarrow \overline{\tau^1 \cup \tau^2}}, \nu) \times_k \begin{bmatrix} \mathbf{U}_{\tau^1, \mathbf{p}_\nu}^{t,k} & \\ & \mathbf{U}_{\tau^2, \mathbf{p}_\nu}^{t,k} \end{bmatrix} \\
 424 \quad (3.9) \quad &\approx \mathcal{K}(\mathbf{t}_{k \leftarrow \overline{\tau}}, \nu) \times_k \left(\mathbf{P}_{\tau,\nu}^{t,k} \begin{bmatrix} \mathbf{U}_{\tau^1, \mathbf{p}_\nu}^{t,k} & \\ & \mathbf{U}_{\tau^2, \mathbf{p}_\nu}^{t,k} \end{bmatrix} \right). \\
 425
 \end{aligned}$$

426 Putting together (3.6), (3.7), (3.8) and (3.9), the proposed tensor butterfly de-
 427 composition can be expressed, for any multi-set $\mathbf{t} = (t_1, t_2, \dots, t_d)$ with t_i at level L^c
 428 of $\mathcal{T}_{t_i^0}$ and any multi-set $\mathbf{s} = (s_1, s_2, \dots, s_d)$ with s_i at level L^c of $\mathcal{T}_{s_i^0}$, by forming a
 429 Tucker-ID for the (\mathbf{t}, \mathbf{s}) pair:

$$\begin{aligned}
 430 \quad (3.10) \quad \mathcal{K}(\mathbf{t}, \mathbf{s}) &\approx \mathcal{K}(\overline{\mathbf{t}}, \overline{\mathbf{s}}) \left(\prod_{k=1}^d \times_k \left(\prod_{l=L^c}^1 \overline{\mathbf{P}}_l^{t,s,k} \overline{\mathbf{U}}^{t,k} \right) \right) \left(\prod_{k=1}^d \times_{d+k} \left(\prod_{l=L^c}^1 \overline{\mathbf{W}}_l^{t,s,k} \overline{\mathbf{V}}^{s,k} \right) \right). \\
 431
 \end{aligned}$$

431 Here, $\bar{\mathbf{t}}$ and $\bar{\mathbf{s}}$ represent the skeleton indices of the Tucker-ID of $\mathcal{K}(\mathbf{t}, \mathbf{s})$. The
 432 interpolation factors $\bar{\mathbf{U}}^{t,k}$ and $\bar{\mathbf{V}}^{s,k}$ in (3.10) are:

433 (3.11)
$$\bar{\mathbf{U}}^{t,k} = \text{diag}_{\tau}(\mathbf{U}_{\tau, \mathbf{s}^0}^{t,k}), \quad \tau \text{ at level } L^c \text{ of } \mathcal{T}_{t_k},$$

434 (3.12)
$$\bar{\mathbf{V}}^{s,k} = \text{diag}_{\nu}(\mathbf{V}_{\mathbf{t}^0, \nu}^{s,k}), \quad \nu \text{ at level } L^c \text{ of } \mathcal{T}_{s_k},$$

436 and the transfer factors $\bar{\mathbf{P}}_l^{t,s,k}$ and $\bar{\mathbf{W}}_l^{t,s,k}$ for $l = 1, \dots, L^c$ are:

437 (3.13)
$$\bar{\mathbf{P}}_l^{t,s,k} = \text{diag}_{\nu} \left(\left[\text{diag}_{\tau}(\mathbf{P}_{\tau, \nu^c}^{t,k}) \right]_c \right), \quad \begin{array}{l} \tau \text{ at level } L^c - l \text{ of } \mathcal{T}_{t_k}, \\ \nu_i \text{ at level } l - 1 \text{ of } \mathcal{T}_{s_i^0}, s_i \subseteq \nu_i, i \leq d; \end{array}$$

438 (3.14)
$$\bar{\mathbf{W}}_l^{t,s,k} = \text{diag}_{\tau} \left(\left[\text{diag}_{\nu}(\mathbf{W}_{\tau^c, \nu}^{s,k}) \right]_c \right), \quad \begin{array}{l} \tau_i \text{ at level } l - 1 \text{ of } \mathcal{T}_{t_i^0}, t_i \subseteq \tau_i, i \leq d, \\ \nu \text{ at level } L^c - l \text{ of } \mathcal{T}_{s_k}. \end{array}$$

440 One can verify that when $d = 1$, the tensor butterfly algorithm (3.10) reduces
 441 to the matrix butterfly algorithm (2.12). But when $d > 1$, the tensor butterfly algo-
 442 rithm has a distinct algorithmic structure so that the corresponding computational
 443 complexity can be significantly reduced compared with the matrix butterfly algorithm.
 444 Detailed computational complexity analysis is provided in subsection 3.2.2.

445 To better understand the structure of the tensor butterfly in (3.10), (3.11), (3.12),
 446 (3.13), and (3.14), we describe its tensor diagram here. We first create the tensor
 447 diagram for a *matrix partitioner* as shown in Figure 3.1(b), which represents a $2^d \times 2$
 448 block partitioning of a matrix such as $\left[\mathbf{W}_{\tau^c, \nu}^{s,k} \right]_c$ in (3.14) for fixed \mathbf{s}, τ, k and ν ,
 449 or $\left[\mathbf{P}_{\tau, \nu^c}^{t,k} \right]_c$ in (3.13) for fixed \mathbf{t}, ν, k and τ . In Figure 3.1(b), each of the row and
 450 column dimensions is connected to a partitioning node. The row partitioning node has
 451 a parent edge with an arrow pointing to the row dimension to be partitioned, and 2
 452 children edges connected to the parent edge. Similarly, the column partitioning node
 453 has a parent edge with an arrow pointing to the column dimension to be partitioned,
 454 and 2^d children edges connected to the parent edge. The weight of the parent edge
 455 (i.e., the number of columns and rows of the matrix) equals the sum of the weights
 456 of the children edges. The diagram in Figure 3.1(c) shows the connectivity for all
 457 $\mathbf{V}_{\mathbf{t}^0, \nu}^{s,k}$ (the green circles) and $\left[\mathbf{W}_{\tau^c, \nu}^{s,k} \right]_c$ (the blue circles) for fixed \mathbf{s} and k . The
 458 multiplication or contraction of all matrices in Figure 3.1(c) results in $\mathbf{V}_{\mathbf{t}, s_k}^{s,k}$ for all
 459 mid-level multi-sets \mathbf{t} , which are of course not explicitly formed.

460 As an example, consider an OIO representing the free-space Green's function in-
 461 teraction between two parallel facing unit square plates in Figure 3.2. The tensor is
 462 $\mathcal{K}(\mathbf{i}, \mathbf{j}) = K(x^i, y^j) = \frac{\exp(-i\omega\rho)}{\rho}$ where $x^i = (\frac{i_1}{n}, \frac{i_2}{n}, 0)$, $y^j = (\frac{j_1}{n}, \frac{j_2}{n}, 1)$, $\rho = |x^i - y^j|$
 463 and ω is the wavenumber. Here 1 represents the distance between the two plates.
 464 Consider an $L=2$ -level tensor butterfly decomposition, with a total of 16 middle-level
 465 multi-set pairs. Let (\mathbf{t}, \mathbf{s}) denote one middle-level multi-set pair with $\mathbf{t} = (t_1, t_2)$ and
 466 $\mathbf{s} = (s_1, s_2)$ as highlighted in orange in Figure 3.2(b). Their children are $t_1^1, t_2^1, t_1^2, t_2^2$
 467 and $s_1^1, s_2^1, s_1^2, s_2^2$. Leveraging the representations in Figure 3.1(b)-(c), the full di-
 468 agram for $\mathcal{K}(\mathbf{t}, \mathbf{s})$ consists of one 4-mode tensor $\mathcal{K}(\bar{\mathbf{t}}, \bar{\mathbf{s}})$ (highlighted in orange in
 469 Figure 3.2(a)), one transfer matrix per mode, and two factor matrices per mode. In
 470 addition, we plot the full connectivity for two other multi-set pairs (highlighted in
 471 green in Figure 3.2(a)). It is important to note that the factor matrices and transfer
 472 matrices are shared among the multi-set pairs.

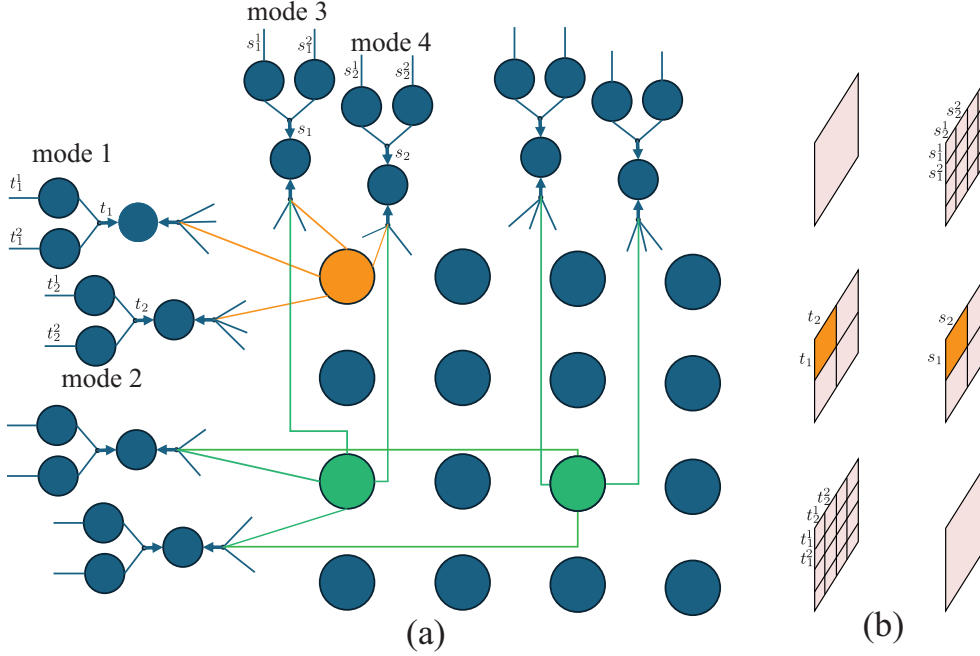


Fig. 3.2: (a) Tensor diagram for the tensor butterfly decomposition of $L = 2$ levels of a 4-mode OIO tensor representing (b) high-frequency Green's function interactions between parallel facing 2D unit squares. Only the full connectivity regarding three middle-level node pairs is shown (the two green circles and one orange circle in (a)). The orange circle in (a) represents the core tensor $\mathcal{K}(\bar{\mathbf{t}}, \bar{\mathbf{s}})$ for a mid-level pair (\mathbf{t}, \mathbf{s}) with $\mathbf{t} = (t_1, t_2)$, $\mathbf{s} = (s_1, s_2)$ highlighted in orange in (b).

473 The proposed tensor butterfly algorithm is fully described in [Algorithm 3.1](#) for a
474 $2d$ -mode tensor $\mathcal{K} \in \mathbb{C}^{m_1 \times m_2 \times \dots \times m_d \times n_1 \times n_2 \times \dots \times n_d}$, which consists of three steps: (1)
475 computation of $\mathbf{V}_{\tau, \nu}^{s, k}$ and $\mathbf{W}_{\tau, \nu}^{s, k}$ starting at Line 1, (2) computation of $\mathbf{U}_{\tau, \nu}^{t, k}$ and $\mathbf{P}_{\tau, \nu}^{t, k}$
476 starting at Line 17, and (3) computation of $\mathcal{K}(\bar{\mathbf{t}}, \bar{\mathbf{s}})$ starting at Line 33. We note that,
477 after each $\mathcal{K}(\bar{\mathbf{t}}, \bar{\mathbf{s}})$ is formed, we leverage floating-point compression tools such as the
478 ZFP software [40] to further compress it.

479 Once \mathcal{K} is compressed, any input tensor $\mathcal{F} \in \mathbb{C}^{n_1 \times n_2 \times \dots \times n_d \times n_v}$ can contract with
480 it to compute $\mathcal{G} = \mathcal{K} \times_{d+1, d+2, \dots, 2d} \mathcal{F}$. It is clear to see that the contraction is
481 equivalent to matrix-matrix multiplication $\mathbf{G} = \mathbf{K}\mathbf{F}$, where $\mathbf{G} \in \mathbb{C}^{\prod_k m_k \times n_v}$, $\mathbf{K} \in$
482 $\mathbb{C}^{\prod_k m_k \times \prod_k n_k}$, and $\mathbf{F} \in \mathbb{C}^{\prod_k n_k \times n_v}$ are matricizations of \mathcal{G} , \mathcal{K} and \mathcal{F} , respectively,
483 and n_v is the number of columns of \mathbf{F} . The contraction algorithm is described in
484 [Algorithm 3.2](#) which consists of three steps:

485 (1) Contraction with $\mathbf{V}_{\tau, \nu}^{s, k}$ and $\mathbf{W}_{\tau, \nu}^{s, k}$. For each level $l = 0, 1, \dots, L^c$, one notices that,
486 since the contraction operation for each multi-set τ with τ_i at level l of \mathcal{T}_i^0 and
487 the middle-level multi-set \mathbf{s} is independent of each other, one needs a separate
488 tensor $\mathcal{F}_{\tau, \mathbf{s}}$ to store the contraction result for each multi-set pair (τ, \mathbf{s}) . $\mathcal{F}_{\tau, \mathbf{s}}$
489 can be computed by mode-by-mode contraction with the factor matrices $\bar{\mathbf{V}}^{s, k}$ for
490 $l = 0$ (Line 6) and the transfer matrices $\text{diag}_\nu(\mathbf{W}_{\tau, \nu}^{s, k})$ for $l > 0$ (Line 8).

491 (2) Contraction with $\mathcal{K}(\bar{\mathbf{t}}, \bar{\mathbf{s}})$ at the middle level. Tensors at the middle level $\mathcal{F}_{\mathbf{t}, \mathbf{s}}$

492 are contracted with each subtensor $\mathcal{K}(\bar{\mathbf{t}}, \bar{\mathbf{s}})$ separately, resulting in tensors $\mathcal{G}_{\mathbf{t}, \mathbf{s}} =$
493 $\mathcal{K}(\bar{\mathbf{t}}, \bar{\mathbf{s}}) \times_{d+1, d+2, \dots, 2d} \mathcal{F}_{\mathbf{t}, \mathbf{s}}$.
494 (3) Contraction with $\mathbf{U}_{\tau, \nu}^{\mathbf{t}, k}$ and $\mathbf{P}_{\tau, \nu}^{\mathbf{t}, k}$. As Step (1), for each level $l = L^c, L^{c-1}, \dots, 0$,
495 the contraction operation for each multi-set ν with ν_i at level l of $\mathcal{T}_{s_i^q}$ and middle-
496 level multi-set \mathbf{t} is independent. At level $l > 0$, the contribution of tensors $\mathcal{G}_{\mathbf{t}, \nu}$ is
497 accumulated into $\mathcal{G}_{\mathbf{t}, p_\nu}$ (Line 26); at level $l = 0$, the contraction results are stored
498 in the final output tensor $\mathcal{G}(\mathbf{t}, 1 : n_\nu)$ (Line 24).

499 **3.2.1. Rank Estimate.** In this subsection, we use two specific high-dimensional
500 examples, namely high-frequency free-space Green's functions for wave equations and
501 uniform discrete Fourier transforms (DFTs) to investigate the matrix and tensor CLR
502 properties, and compare the matrix and tensor butterfly ranks r_m and r_t , respectively.
503 For the Green's function example, the tensor CLR property is a result of matrix CLR
504 and translational invariance, and r_t is much smaller than r_m ; for the DFT example, the
505 tensor CLR property is a result of matrix CLR and dimensionality separability, and
506 r_t is exactly the same as r_m of 1D DFTs. For more-general OIOs, such as analytical
507 and numerical Green's functions for inhomogeneous media, Radon transforms, non-
508 uniform DFTs, and general Fourier integral operators, rigorous rank analysis is non-
509 trivial and we rely on numerical experiments in section 4 to demonstrate the efficacy
510 of the tensor butterfly algorithm.

511 *High-frequency Green's functions.* We use an example similar to the one used
512 in subsection 3.2. Consider an OIO representing the free-space Green's function in-
513 teraction between two parallel-facing unit-square plates. The $n \times n \times n \times n$ tensor
514 is

$$515 \quad (3.15) \quad \mathcal{K}(\mathbf{i}, \mathbf{j}) = K(x^{\mathbf{i}}, y^{\mathbf{j}}) = \frac{\exp(-i\omega\rho)}{\rho},$$

516 where $x^{\mathbf{i}} = (\frac{i_1}{n}, \frac{i_2}{n}, 0)$, $y^{\mathbf{j}} = (\frac{j_1}{n}, \frac{j_2}{n}, \rho_{\min})$, ω is the wavenumber, and $\rho = |x^{\mathbf{i}} - y^{\mathbf{j}}|$. Here
517 ρ_{\min} represents the distance between the two plates assumed to be sufficiently large.
518 In the high-frequency setting, $n = C_p\omega$ with a constant C_p independent of n and ω ,
519 and the grid size is $\delta_x = \delta_y = \frac{1}{n}$ per dimension. It has been well studied [53, 54, 20, 5]
520 that for any multi-set pair (τ, ν) (assuming that each set of the multi-set τ or ν
521 contains contiguous indices) leading to a subtensor $\mathcal{K}(\tau, \nu)$ of sizes $m_1 \times m_2 \times n_1 \times n_2$
522 with $m_i, n_i \leq n$, the numerical rank of its matricization $\mathbf{K} \in \mathbb{C}^{m_1 m_2 \times n_1 n_2}$ can be
523 estimated as

$$524 \quad (3.16) \quad r_m \approx \omega^2 a^2 \theta \phi + \Delta_\epsilon \approx \frac{\omega^2 a^2 n_1 n_2}{n^2 \rho_{\min}^2} + \Delta_\epsilon.$$

525 Here a is the radius of the sphere enclosing the target domain of physical sizes $m_1 \delta_x \times$
526 $m_2 \delta_y$. $\theta \approx \frac{n_1}{n \rho_{\min}}$, $\phi \approx \frac{n_2}{n \rho_{\min}}$, and the product $\theta \phi$ represents the solid angle covered
527 by the source domain as seen from the center of the target domain. Note that $\frac{\omega a}{\rho_{\min}}$
528 approximately represents the Nyquist sampling rate per direction needed in the source
529 domain. The ϵ -dependent term $\Delta_\epsilon = O(\log \epsilon^{-1})$ according to analysis in [53, 54]. The
530 matrix and tensor butterfly ranks can be estimated as follows:

531 • *Matrix butterfly rank:* Consider a matrix butterfly factorization of matricization of
532 \mathcal{K} . By design, for any node pair at each level, $m_1 n_1 = m_2 n_2 = C_b n$, where C_b^2
533 represents the size of the leaf nodes. Therefore, the matrix butterfly rank can be
534 estimated from (3.16) as

$$535 \quad (3.17) \quad r_m \approx \frac{C_b^2}{2C_p^2 \rho_{\min}^2} + \Delta_\epsilon.$$

Algorithm 3.1 Construction algorithm for the tensor butterfly decomposition of a $2d$ -mode tensor $\mathcal{K} \in \mathbb{C}^{m_1 \times m_2 \times \dots \times m_d \times n_1 \times n_2 \times \dots \times n_d}$

Input: A function to evaluate a $2d$ -mode tensor $\mathcal{K}(\mathbf{i}, \mathbf{j})$ for arbitrary multi-indices (\mathbf{i}, \mathbf{j}) , binary partitioning trees of L levels $\mathcal{T}_{t_k^0}$ and $\mathcal{T}_{s_k^0}$ with roots $t_k^0 = \{1, 2, \dots, m_k\}$ and $s_k^0 = \{1, 2, \dots, n_k\}$, a relative compression tolerance ϵ .

Output: Tensor butterfly decomposition of \mathcal{K} : (1) $\mathbf{V}_{\tau, \nu}^{s, k}$ at $l = 0$ and $\mathbf{W}_{\tau, \nu}^{s, k}$ at $1 \leq l \leq L^c$ of $k \leq d$ for multi-set τ with node τ_i at level l of $\mathcal{T}_{t_i^0}$, multi-set s with node s_i at level L^c of $\mathcal{T}_{s_i^0}$, and node ν at level $L^c - l$ of subtree \mathcal{T}_{s_k} , (2) $\mathbf{U}_{\tau, \nu}^{t, k}$ at $l = 0$ and $\mathbf{P}_{\tau, \nu}^{t, k}$ at $1 \leq l \leq L^c$ of $k \leq d$ for multi-set ν with node ν_i at level l of $\mathcal{T}_{s_i^0}$, multi-set t with node t_i at level L^c of $\mathcal{T}_{t_i^0}$, and node τ at level $L^c - l$ of subtree \mathcal{T}_{t_k} , and (3) subtensors $\mathcal{K}(\bar{\mathbf{t}}, \bar{\mathbf{s}})$ at $l = L^c$.

```

1: (1) Compute  $\mathbf{V}_{\tau, \nu}^{s, k}$  and  $\mathbf{W}_{\tau, \nu}^{s, k}$ :
2: for level  $l = 0, \dots, L^c$  do
3:   for multi-set  $s = (s_1, \dots, s_d)$  with  $s_i$  at level  $L^c$  of  $\mathcal{T}_{s_i^0}$  do
4:     for multi-set  $\tau = (\tau_1, \tau_2, \dots, \tau_d)$  with  $\tau_i$  at level  $l$  of  $\mathcal{T}_{t_i^0}$  do
5:       for mode index  $k = 1, \dots, d$  do
6:         for node  $\nu$  at level  $L^c - l$  of  $\mathcal{T}_{s_k}$  do
7:           if  $l = 0$  then ▷ Use (3.6) with proxies  $\hat{\tau}, \hat{s}$  and tolerance  $\epsilon$ 
8:             Compute  $\mathbf{V}_{\tau, \nu}^{s, k}$  and  $\bar{\nu}$  via mode- $(d + k)$  unfolding of  $\mathcal{K}(\hat{\tau}, \hat{s}_{k \leftarrow \nu})$ 
9:           else ▷ Use (3.8) with proxies  $\hat{\tau}, \hat{s}$  and tolerance  $\epsilon$ 
10:            Compute  $\mathbf{W}_{\tau, \nu}^{s, k}$  and  $\bar{\nu}$  via mode- $(d + k)$  unfolding of
11:               $\mathcal{K}(\hat{\tau}, \hat{s}_{k \leftarrow \nu^1 \cup \nu^2})$ 
12:            end if
13:          end for
14:        end for
15:      end for
16:    end for
17: (2) Compute  $\mathbf{U}_{\tau, \nu}^{t, k}$  and  $\mathbf{P}_{\tau, \nu}^{t, k}$ :
18: for level  $l = 0, \dots, L^c$  do
19:   for multi-set  $t = (t_1, \dots, t_d)$  with  $t_i$  at level  $L^c$  of  $\mathcal{T}_{t_i^0}$  do
20:     for multi-set  $\nu = (\nu_1, \nu_2, \dots, \nu_d)$  with  $\nu_i$  at level  $l$  of  $\mathcal{T}_{s_i^0}$  do
21:       for mode index  $k = 1, \dots, d$  do
22:         for node  $\tau$  at level  $L^c - l$  of  $\mathcal{T}_{t_k}$  do
23:           if  $l = 0$  then ▷ Use (3.7) with proxies  $\hat{t}, \hat{\nu}$  and tolerance  $\epsilon$ 
24:             Compute  $\mathbf{U}_{\tau, \nu}^{t, k}$  and  $\bar{\tau}$  via mode- $k$  unfolding of  $\mathcal{K}(\hat{t}_{k \leftarrow \tau}, \hat{\nu})$ 
25:           else ▷ Use (3.9) with proxies  $\hat{t}, \hat{\nu}$  and tolerance  $\epsilon$ 
26:             Compute  $\mathbf{P}_{\tau, \nu}^{t, k}$  and  $\bar{\tau}$  via mode- $k$  unfolding of  $\mathcal{K}(\hat{t}_{k \leftarrow \tau^1 \cup \tau^2}, \hat{\nu})$ 
27:           end if
28:         end for
29:       end for
30:     end for
31:   end for
32: end for
33: (3) Compute  $\mathcal{K}(\bar{\mathbf{t}}, \bar{\mathbf{s}})$ :
34: for multi-set  $s = (s_1, \dots, s_d)$  with  $s_i$  at level  $L^c$  of  $\mathcal{T}_{s_i^0}$  do
35:   for multi-set  $t = (t_1, \dots, t_d)$  with  $t_i$  at level  $L^c$  of  $\mathcal{T}_{t_i^0}$  do
36:     Compute  $\mathcal{K}(\bar{\mathbf{t}}, \bar{\mathbf{s}})$  and ZFP compress it
37:   end for
38: end for

```

Algorithm 3.2 Contraction algorithm for a tensor butterfly decomposition with an input tensor

Input: The tensor butterfly decomposition of a $2d$ -mode tensor

$\mathcal{K} \in \mathbb{C}^{m_1 \times m_2 \times \dots \times m_d \times n_1 \times n_2 \times \dots \times n_d}$, and a (full) $d + 1$ -mode input tensor

$\mathcal{F} \in \mathbb{C}^{n_1 \times n_2 \times \dots \times n_d \times n_v}$ where n_v denotes the number of columns of $\mathbf{F}^{(d+1)}$.

Output: The $d + 1$ -mode output tensor $\mathcal{G} = \mathcal{K} \times_{d+1, d+2, \dots, 2d} \mathcal{F}$ where $\mathcal{G} \in \mathbb{C}^{m_1 \times m_2 \times \dots \times m_d \times n_v}$.

```

1: (1) Multiply with  $\mathbf{V}_{\tau, \nu}^{s, k}$  and  $\mathbf{W}_{\tau, \nu}^{s, k}$ :
2: for level  $l = 0, \dots, L^c$  do
3:   for multi-set  $\mathbf{s} = (s_1, s_2, \dots, s_d)$  with  $s_i$  at level  $L^c$  of  $\mathcal{T}_{s_i^0}$  do
4:     for multi-set  $\boldsymbol{\tau} = (\tau_1, \tau_2, \dots, \tau_d)$  with  $\tau_i$  at level  $l$  of  $\mathcal{T}_{\tau_i^0}$  do
5:       if  $l = 0$  then
6:          $\mathcal{F}_{\boldsymbol{\tau}, \mathbf{s}} = \mathcal{F}(\mathbf{s}, 1 : n_v) \prod_{k=1}^d \times_k \overline{\mathbf{V}}^{s, k}$ 
7:       else
8:          $\mathcal{F}_{\boldsymbol{\tau}, \mathbf{s}} = \mathcal{F}_{\mathbf{p}_{\boldsymbol{\tau}}, \mathbf{s}} \prod_{k=1}^d \times_k \text{diag}_{\nu}(\mathbf{W}_{\tau, \nu}^{s, k})$   $\triangleright \nu$  at level  $L^c - l$  of  $\mathcal{T}_{s_k}$ 
9:       end if
10:    end for
11:  end for
12: end for
13: (2) Contract with  $\mathcal{K}(\overline{\mathbf{t}}, \overline{\mathbf{s}})$ :
14: for multi-set  $\mathbf{t} = (t_1, t_2, \dots, t_d)$  with  $t_i$  at level  $L^c$  of  $\mathcal{T}_{t_i^0}$  do
15:   for multi-set  $\mathbf{s} = (s_1, s_2, \dots, s_d)$  with  $s_i$  at level  $L^c$  of  $\mathcal{T}_{s_i^0}$  do
16:     ZFP decompress  $\mathcal{K}(\overline{\mathbf{t}}, \overline{\mathbf{s}})$  and compute  $\mathcal{G}_{\mathbf{t}, \mathbf{s}} = \mathcal{K}(\overline{\mathbf{t}}, \overline{\mathbf{s}}) \times_{d+1, d+2, \dots, 2d} \mathcal{F}_{\mathbf{t}, \mathbf{s}}$ 
17:   end for
18: end for
19: (3) Multiply with  $\mathbf{U}_{\tau, \nu}^{t, k}$  and  $\mathbf{P}_{\tau, \nu}^{t, k}$ :
20: for level  $l = L^c, \dots, 0$  do
21:   for multi-set  $\mathbf{t} = (t_1, t_2, \dots, t_d)$  with  $t_i$  at level  $L^c$  of  $\mathcal{T}_{t_i^0}$  do
22:     for multi-set  $\boldsymbol{\nu} = (\nu_1, \nu_2, \dots, \nu_d)$  with  $\nu_i$  at level  $l$  of  $\mathcal{T}_{\nu_i^0}$  do
23:       if  $l = 0$  then  $\triangleright$  Compute and return  $\mathcal{G}$ 
24:          $\mathcal{G}(\mathbf{t}, 1 : n_v) = \mathcal{G}_{\mathbf{t}, \boldsymbol{\nu}} \prod_{k=1}^d \times_k \overline{\mathbf{U}}^{t, k}$ 
25:       else
26:          $\mathcal{G}_{\mathbf{t}, \mathbf{p}_{\boldsymbol{\nu}}} += \mathcal{G}_{\mathbf{t}, \boldsymbol{\nu}} \prod_{k=1}^d \times_k \text{diag}_{\tau}(\mathbf{P}_{\tau, \nu}^{t, k})$   $\triangleright \tau$  at level  $L^c - l$  of  $\mathcal{T}_{t_k}$ 
27:       end if
28:     end for
29:   end for
30: end for

```

536 Here we have assumed $a = \frac{m_1}{\sqrt{2n}}$. Note that r_m is a constant independent of n , and
537 therefore the matrix CLR property holds true.

538 • *Tensor butterfly rank:* Consider an L -level tensor butterfly factorization of \mathcal{K} . We
539 just need to check the tensor rank, e.g., the rank of the mode-4 unfolding of the
540 corresponding subtensors at Step (1) of [Algorithm 3.1](#), as the unfolding for the
541 other modes can be investigated in a similar fashion. [Figure 3.3\(a\)](#) shows an exam-
542 ple of $L = 2$, where the target and source domains are partitioned at $l = 0$ (top)
543 and $l = L^c = 1$ (bottom) at Step (1) of [Algorithm 3.1](#). Consider a multi-set pair
544 $(\boldsymbol{\tau}, \mathbf{s}_{k \leftarrow \nu})$ with $k = 4$ required by the tensor CLR property in (3.6). [Figure 3.3\(a\)](#)
545 highlights in orange one multi-set pair at $l = 0$ (top) and one multi-set pair at
546 $l = L^c$ (bottom). Mode 4 is highlighted in green (in all subfigures of [Figure 3.3](#)),
547 which needs to be skeletonized by ID. By (3.16), the rank of the matricization of

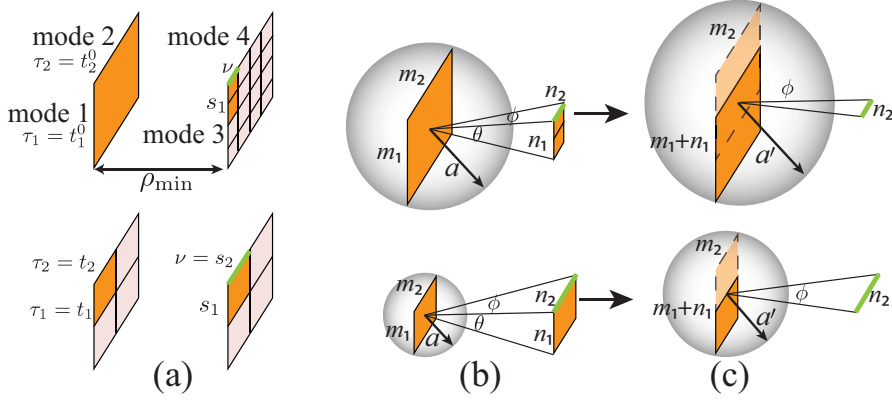


Fig. 3.3: Illustration of the tensor CLR property with $L = 2$ for a 4-mode tensor representing free-space Green's function interactions between parallel facing unit square plates. (a) The target and source domains are partitioned at $l = 0$ (top) and $l = L^c = 1$ (bottom) with a multi-set pair $(\tau, \mathbf{s}_{k \leftarrow \nu})$ highlighted in orange for the skeletonization along mode 4. The sizes of the nodes are $|\tau_1| = m_1, |\tau_2| = m_2, |s_1| = n_1$ and $|\nu| = n_2$. (b) Illustration of the rank of the matricization of $\mathcal{K}(\tau, \mathbf{s}_{k \leftarrow \nu})$ used in the matrix butterfly algorithm. Here a is the radius of the sphere enclosing the target domain of physical sizes $m_1 \delta_x \times m_2 \delta_y$. $\theta \approx \frac{n_1}{n \rho_{\min}}$, $\phi \approx \frac{n_2}{n \rho_{\min}}$, and the product $\theta \phi$ represents the solid angle covered by the source domain as seen from the center of the target domain. (c) Illustration of the rank of the mode-4 unfolding of $\mathcal{K}(\tau, \mathbf{s}_{k \leftarrow \nu})$ used in the tensor butterfly algorithm. Here, a' is the radius of the sphere enclosing the enlarged target domain. The source domain is reduced to a line segment of length $n_2 \delta_y$.

548 $\mathcal{K}(\tau, \mathbf{s}_{k \leftarrow \nu})$ is no longer a constant as the tensor butterfly algorithm needs to keep
549 $n_1 = |s_1| = n/2^{L^c}$ (see Figure 3.3(b)). However, due to translational invariance of
550 the free-space Green's function, i.e., $K(x^i, y^j) = K(\tilde{x}, \tilde{y})$, where $\tilde{x} = (0, \frac{i_2}{n}, 0)$,
551 $\tilde{y} = (\frac{j_1 - i_1}{n}, \frac{j_2}{n}, \rho_{\min})$, the mode-4 unfolding of $\mathcal{K}(\tau, \mathbf{s}_{k \leftarrow \nu})$ is the matrix represent-
552 ing the Green's function interaction between an enlarged target domain of sizes
553 $(m_1 + n_1) \delta_x \times m_2 \delta_y$ and a source line segment of length $n_2 \delta_y$. Therefore its rank
554 (hence the tensor rank) can be estimated as

$$555 \quad (3.18) \quad r_t \approx \omega a' \phi + \Delta_\epsilon \approx \frac{\omega a' n_2}{n \rho_{\min}} + \Delta_\epsilon \leq \frac{\sqrt{2} C_b}{C_p \rho_{\min}} + \Delta_\epsilon,$$

556 where a' is the radius of the sphere enclosing the enlarged target domain and $\frac{\omega a'}{\rho_{\min}}$
557 approximately represents the Nyquist sampling rate on the source line segment.
558 The last inequality is a result of $a' \approx \frac{m_1 + n_1}{\sqrt{2} n} \leq \frac{\sqrt{2} m_1}{n}$ and $m_2 n_2 = C_b n$. Here, the
559 critical condition $n_1 \leq m_1$ is a direct result of the setup of the tensor CLR in (3.6):
560 $l \leq L^c$ and $n_1 = |s_1| = n/2^{L^c}$ (i.e., s_1 is fixed as the middle level set as l changes).
561 One can clearly see from (3.18) that r_t is independent of n , and thus the tensor
562 CLR property holds true.

563 We remark that the tensor butterfly rank r_t in (3.18) is significantly smaller
564 than the matrix butterfly rank r_m in (3.17) with $r_t \approx 2\sqrt{r_m}$. One can perform similar
565 analysis of r_m and r_t for different geometrical settings, such as a pair of well-separated
566 3D unit cubes, or a pair of co-planar 2D unit-square plates. We leave these exercises

567 to the readers.

568 *Discrete Fourier Transform.* Our second example is the high-dimensional discrete
569 Fourier transform (DFT) defined by

$$570 \quad (3.19) \quad \mathcal{K}(\mathbf{i}, \mathbf{j}) = \exp(2\pi i \mathbf{x}^{\mathbf{i}} \cdot \mathbf{y}^{\mathbf{j}})$$

571 with $\mathbf{x}^{\mathbf{i}} = (i_1 - 1, i_2 - 1, \dots, i_d - 1)$ and $\mathbf{y}^{\mathbf{j}} = (\frac{j_1-1}{n}, \frac{j_2-1}{n}, \dots, \frac{j_d-1}{n})$. We first notice
572 that, since

$$573 \quad (3.20) \quad \exp(2\pi i \mathbf{x}^{\mathbf{i}} \cdot \mathbf{y}^{\mathbf{j}}) = \prod_{k=1}^d \exp\left(\frac{2\pi i (i_k - 1)(j_k - 1)}{n}\right),$$

574 to carry out arbitrary high-dimensional DFTs one can simply perform 1D DFTs one
575 dimension at a time (while fixing the indices of the other dimensions) by either 1D
576 FFT or 1D matrix butterfly algorithms. We choose the 1D butterfly approach as our
577 reference algorithm. For each node pair at dimension k discretized into a $m_k \times n_k$
578 matrix, we assume that $m_k n_k = C_b n$. It has been proved in [8, 70] that this leads to
579 the matrix CLR property and each 1D DFT (fixing indices in other dimensions) can
580 be computed by the matrix butterfly algorithm in $O(n \log n)$ time with a constant
581 butterfly rank r_m . Overall this approach requires $O(dn^d \log n)$ operations.

582 In contrast, the tensor butterfly algorithm relies on direct compression of e.g.,
583 mode- k unfolding of subtensors $\mathcal{K}(\boldsymbol{\tau}, \mathbf{s}_{k \leftarrow \nu})$. Consider any submatrix $\mathbf{K}_{sub} \in \mathbb{C}^{m_k \times n_k}$
584 of this unfolding matrix $\mathbf{K}^{(k)}$; by fixing i_p and j_p with $p \neq k$, its entry is simply

$$585 \quad \exp\left(\frac{2\pi i (i_k - 1)(j_k - 1)}{n}\right)$$

586 scaled by a constant factor

$$587 \quad \prod_{p \neq k} \exp\left(\frac{2\pi i (i_p - 1)(j_p - 1)}{n}\right)$$

588 of modulus 1. Therefore the tensor butterfly rank is

$$589 \quad (3.21) \quad r_t = \text{rank}(\mathbf{K}^{(k)}) = \text{rank}(\mathbf{K}_{sub}) = r_m.$$

590 The tensor CLR property thus holds true, and the tensor rank is exactly the same as
591 the 1D butterfly algorithm per dimension. However, as we will see [subsection 3.2.2](#),
592 our tensor butterfly algorithm yields a linear instead of quasi-linear CPU complexity
593 for high-dimensional DFTs.

594 **3.2.2. Complexity Analysis.** Here we provide an analysis of computational
595 complexity and memory requirement of the proposed construction algorithm ([Al-](#)
596 [gorithm 3.1](#)) and contraction algorithm ([Algorithm 3.2](#)), assuming that the tensor
597 butterfly rank r_t is a small constant and $d > 1$. Recall that the $2d$ -mode tensor \mathcal{K}
598 has size n and a binary tree ($\mathcal{T}_{i_k}^L$ or $\mathcal{T}_{s_k}^L$) of L levels along each mode k . $L^c = L/2$
599 denotes the middle level. We refer the readers to [Table 2.1](#) to recall the notations of
600 the multi-set, k^{th} set, mid-level subtensor, transfer matrix, and interpolation matrix,
601 etc.

602 At Step (1) of [Algorithm 3.1](#), each level $1 \leq l \leq L^c$ has $\#\mathbf{s} = O(\sqrt{n}^d)$, $\#\boldsymbol{\tau} = 2^{dl}$,
603 $\#\nu = O(\sqrt{n}/2^l)$ for each mode $k \leq d$. Each $\mathbf{W}_{\boldsymbol{\tau}, \nu}^{\mathbf{s}, k}$ requires $O(r_t^2)$ storage, and

604 $O(r_t^{2d+1})$ computational time when proxy indices $\hat{\tau}$, \hat{s} are being used. The storage
 605 requirement and computational cost for $\mathbf{W}_{\tau,\nu}^{s,k}$ are:

$$606 \quad (3.22) \quad \text{mem}_W = \sum_{l=1}^{L^c} dO(\sqrt{n^d})2^{dl}O(\sqrt{n}/2^l)O(r_t^2) = O(dn^d r_t^2),$$

$$607 \quad (3.23) \quad \text{time}_W = \sum_{l=1}^{L^c} dO(\sqrt{n^d})2^{dl}O(\sqrt{n}/2^l)O(r_t^{2d+1}) = O(dn^d r_t^{2d+1}).$$

608

609 One can easily verify that the computation and storage of $\mathbf{V}_{\tau,\nu}^{s,k}$ at $l = 0$ is less
 610 dominant than $\mathbf{W}_{\tau,\nu}^{s,k}$ at $l > 0$ and we skip its analysis.

611 At Step (2) of [Algorithm 3.1](#), we have $\#\mathbf{s} = O(\sqrt{n^d})$ and $\#\mathbf{t} = O(\sqrt{n^d})$, and
 612 each $\mathcal{K}(\bar{\mathbf{t}}, \bar{\mathbf{s}})$ requires $O(r_t^{2d})$ computation time and storage units (even if it is further
 613 ZFP compressed to reduce storage requirement), which adds up to

$$614 \quad (3.24) \quad \text{mem}_K = O(\sqrt{n^d})O(\sqrt{n^d})O(r_t^{2d}) = O(n^d r_t^{2d}),$$

$$615 \quad (3.25) \quad \text{time}_K = O(\sqrt{n^d})O(\sqrt{n^d})O(r_t^{2d}) = O(n^d r_t^{2d}).$$

617 Step (3) of [Algorithm 3.1](#) has similar computational cost and memory requirement
 618 to Step (1) when contracting with the intermediate matrices $\mathbf{P}_{\tau,\nu}^{t,k}$, with $\text{mem}_P \sim$
 619 mem_W and $\text{time}_P \sim \text{time}_W$.

620 Overall, [Algorithm 3.1](#) requires

$$621 \quad (3.26) \quad \text{mem} = \text{mem}_W + \text{mem}_K + \text{mem}_P = O(n^d r_t^{2d}),$$

$$622 \quad (3.27) \quad \text{time} = \text{time}_W + \text{time}_K + \text{time}_P = O(dn^d r_t^{2d+1}).$$

624 Following a similar analysis, one can estimate the computational cost of [Algo-](#)
 625 [rithm 3.2](#) as $O(n^d r_t^{2d} n_v)$, which is essentially of the similar order as mem of [Algo-](#)
 626 [rithm 3.1](#), except an extra factor n_v representing the size of the last dimension of the
 627 input tensor.

628 One critical observation is that the time and storage complexity of the tensor
 629 butterfly algorithm is *linear* in n^d with smaller ranks r_t , while that of the matrix
 630 butterfly algorithm is *quasi-linear* in n^d with much larger ranks r_m . This leads to a
 631 significantly superior algorithm, as will be demonstrated with the numerical results
 632 in [section 4](#). That being said, one can verify that there is no difference between the
 633 two algorithms when $d = 1$.

634 **3.2.3. Comparison with Tucker-ID and QTT.** Here we make a comparison
 635 of the computational complexities of the matrix butterfly algorithm, tensor butterfly
 636 algorithm, Tucker-ID and QTT for several frequently encountered OIOs with $d = 2, 3$,
 637 namely Green's functions for high-frequency wave equations (where $d = 2$ represents
 638 two parallel facing unit square plates and $d = 3$ represents two separated unit cubes),
 639 Radon transforms (a type of Fourier integral operators), and DFT. We first summarize
 640 the computational complexities of the factorization and application of matrix and
 641 tensor butterfly algorithms in [Table 3.1](#). Here we use r to denote the maximum rank
 642 of the submatrices or (unfolding and matricization of) subtensors associated with each
 643 algorithm. In other words, we drop the subscript of r_m and r_t in this subsection. We
 644 note that $r = O(1)$ for butterfly algorithms, and the computational complexity for
 645 matrix and tensor butterfly algorithms is, respectively, $O(dn^d \log n)$ and $O(dn^d)$, for
 646 all OIOs considered here.

Algorithm	Factor time		Apply time		r	
	$d = 2$	$d = 3$	$d = 2$	$d = 3$	$d = 2$	$d = 3$
Tensor butterfly	n^2	n^3	n^2	n^3	1	1
Matrix butterfly	$n^2 \log n$	$n^3 \log n$	$n^2 \log n$	$n^3 \log n$	1	1
Tucker-ID	n^4	$n^4 - n^{6*}$	n^4	$n^4 - n^{6*}$	n	n
QTT (Green&Radon)	$n^3 \log n$	$n^3 \log n$	$n^4 \log n$	$n^5 \log n$	n	n
QTT (DFT)	$\log n$	$\log n$	$n^2 \log n$	$n^3 \log n$	1	1

Table 3.1: CPU complexity of the tensor butterfly algorithm, matrix butterfly algorithm, Tucker-ID and QTT when applied to high-frequency Green’s functions ($d = 2$ represents two parallel facing unit square plates and $d = 3$ represents two separated unit cubes), DFT and Radon transforms. Here we assume that tensor butterfly, matrix butterfly and Tucker-ID algorithms use proxy indices, and the QTT algorithm uses TT-cross. The big O notation is assumed. *: for $d = 3$, the complexity of Tucker-ID is n^6 for Radon transform and DFT, and n^4 for Green’s function.

647 The Tucker-ID algorithm in [subsection 3.1](#) (even with the use of proxy indices
648 to accelerate the factorization), always leads to $r = O(n)$ for OIOs and hence almost
649 always $O(n^{2d})$ factorization and application complexities (see [Table 3.1](#)). One excep-
650 tion is perhaps the Green’s function for $d = 3$, where one can easily show that 4 out of
651 the 6 unfolding matrices have a rank of $O(n)$ and the remaining 2 have a rank of $O(1)$,
652 leading to the $O(n^4)$ computational complexity. Overall, we remark that Tucker-type
653 decomposition algorithms are typically the least efficient tensor algorithms for OIOs.

654 The QTT algorithm, on the other hand, is a more subtle algorithm to compare
655 with. Assuming that the maximum rank among all steps in QTT is r , we first summa-
656 rize the computational complexities of the factorization and application of QTT. For
657 factorization, we only consider the TT-cross type of algorithms, which yields the best
658 known computational complexity among all TT-based algorithms. The computational
659 complexity of TT-cross is $O(dr^3 \log n)$ [[14](#), [57](#)]. Once factorized, the application cost
660 of the QTT factorization with a full input tensor is $O(dr^2 n^d \log n)$ [[14](#)]. This com-
661 plexity can be reduced to $O(dr^2 r_i^2 \log n)$ when the input tensor is also in the QTT
662 format with TT rank r_i . However, an arbitrary input tensor can have a TT rank up
663 to $r_i = O(n^{d/2})$ (which leads to the same application cost as contraction with a full
664 input tensor). Therefore in our comparative study, we stick with the $O(dr^2 n^d \log n)$
665 application complexity.

666 For high-frequency Green’s functions and general-form Fourier integral operators
667 (e.g. Radon transforms), the TT rank in general behaves as $r = O(n)$ [[14](#)], leading
668 to a factorization cost of $O(dn^3 \log n)$ and an application cost of $O(dn^{2+d} \log n)$, as
669 detailed in [Table 3.1](#). It is worth mentioning that, treating DFTs as a special type
670 of Fourier integral operators, QTT can achieve $r = O(1)$ when a proper bit-reversal
671 ordering is used [[9](#)], leading to a factorization cost of $O(d \log n)$ and an application
672 cost of $O(dn^d \log n)$, as shown in [Table 3.1](#). In contrast, the proposed tensor butterfly
673 algorithm can always yield $O(dn^d)$ factorization and $O(n^d)$ application costs.

674 **4. Numerical Results.** This section provides several numerical examples to
675 demonstrate the accuracy and efficiency of the proposed tensor butterfly algorithm
676 when applied to large-scale and high-dimensional OIOs including Green’s function
677 tensors for high-frequency Helmholtz equations ([subsection 4.1](#)), Radon transform
678 tensors ([subsection 4.2](#)), and high-dimensional DFTs ([subsection 4.3](#)). We compare

679 our algorithm with a few existing matrix and tensor algorithms including the matrix
680 butterfly algorithm in [subsection 2.2](#), the Tucker-ID algorithm in [subsection 3.1](#), the
681 QTT algorithm [57], the FFT algorithm implemented in the heFFTe package [1], and
682 the non-uniform FFT (NUFFT) algorithm implemented in the FINUFFT package
683 [2]. All of these algorithms except for Tucker-ID (sequential implementation in For-
684 tran2008 via the ButterflyPACK package [46]) and FINUFFT (Python interface to
685 the C backend with shared-memory parallelism) are tested in distributed-memory par-
686 allelism. The reference binary-tree-based matrix butterfly algorithm in [subsection 2.2](#)
687 is implemented in Fortran2008 with distributed-memory parallelism [47], available in
688 the ButterflyPACK package [46]. The proposed tensor butterfly algorithm is also
689 available in the ButterflyPACK package with distributed-memory parallelism (which
690 will be described in detail in a future paper). The matrix and tensor butterfly al-
691 gorithms leverage ZFP to further compress the middle-level submatrices and subten-
692 sors, respectively. It is worth noting that currently there is no single package that
693 can both compute and apply the QTT decomposition in distributed-memory parallel-
694 ism. In our tests, we perform the factorization using a distributed-memory TT code
695 (fully Python) [63] that parallelizes a cross interpolation algorithm [19], and then we
696 implement the distributed-memory QTT contraction via the CTF package (Python
697 interface to the C++ backend) [64]. All experiments are performed using 4 CPU
698 nodes of the Perlmutter machine at NERSC in Berkeley, where each node has two
699 64-core AMD EPYC 7763 processors and 128GB of 2133MHz DDR4 memory.

700 **4.1. Green’s functions for high-frequency Helmholtz equations.** In this
701 subsection, we consider the tensor discretized from 3D free-space Green’s functions
702 for high-frequency Helmholtz equations. Specifically, the tensor entry is

$$703 \quad (4.1) \quad \mathcal{K}(i, j) = \frac{\exp(-i\omega\rho)}{\rho}, \quad \rho = |x^i - y^j|,$$

704 where ω represents the wave number. Two tests are performed: (1) A 4-way tensor
705 representing the Green’s function interaction between two parallel facing unit plates
706 with distance 1, i.e., $x^i = (\frac{i_1}{n}, \frac{i_2}{n}, 0)$, $y^j = (\frac{j_1}{n}, \frac{j_2}{n}, 1)$, and $d = 2$. (2) A 6-way tensor
707 representing the Green’s function interaction between two unit cubes with the distance
708 between their centers set to 2, i.e., $x^i = (\frac{i_1}{n}, \frac{i_2}{n}, \frac{i_3}{n})$, $y^j = (\frac{j_1}{n}, \frac{j_2}{n}, \frac{j_3}{n} + 2)$, and $d = 3$. For
709 both tests, the wave number is chosen such that the number of points per wave length
710 is 4, i.e., $2\pi n/\omega = 4$ or $C_p = 2/\pi$. We first perform compression using the tensor
711 butterfly, Tucker-ID and QTT algorithms, and then perform application/contraction
712 using a random input tensor \mathcal{F} . We also add results for the matrix butterfly algorithm
713 using the corresponding matricization of \mathcal{K} and \mathcal{F} .

714 [Figure 4.1](#) (left) shows the factorization time, application time and memory usage
715 of each algorithm using a compression tolerance $\epsilon = 10^{-6}$ for the parallel plate case.
716 For QTT, we show the memory of the factorization (labeled as “QTT(Factor)”) and
717 application (labeled as “QTT(Apply)”) separately. Note that although QTT factor-
718 ization requires sub-linear memory usage, QTT contraction becomes super-linear due
719 to the full QTT rank of the input tensor. Overall, we achieve the expected complex-
720 ities listed in [Table 3.1](#) for the butterfly and Tucker-ID algorithms. For QTT,
721 however, instead of an $O(n)$ rank scaling, we observe an $O(n^{3/4})$ rank scaling, leading
722 to slightly better complexities compared with [Table 3.1](#). We leave this as a future
723 investigation. That said, the tensor butterfly algorithm achieves the linear CPU
724 and memory complexities for both factorization and application with a much smaller
725 prefactor compared to all the other algorithms. Remarkably, the tensor butterfly al-

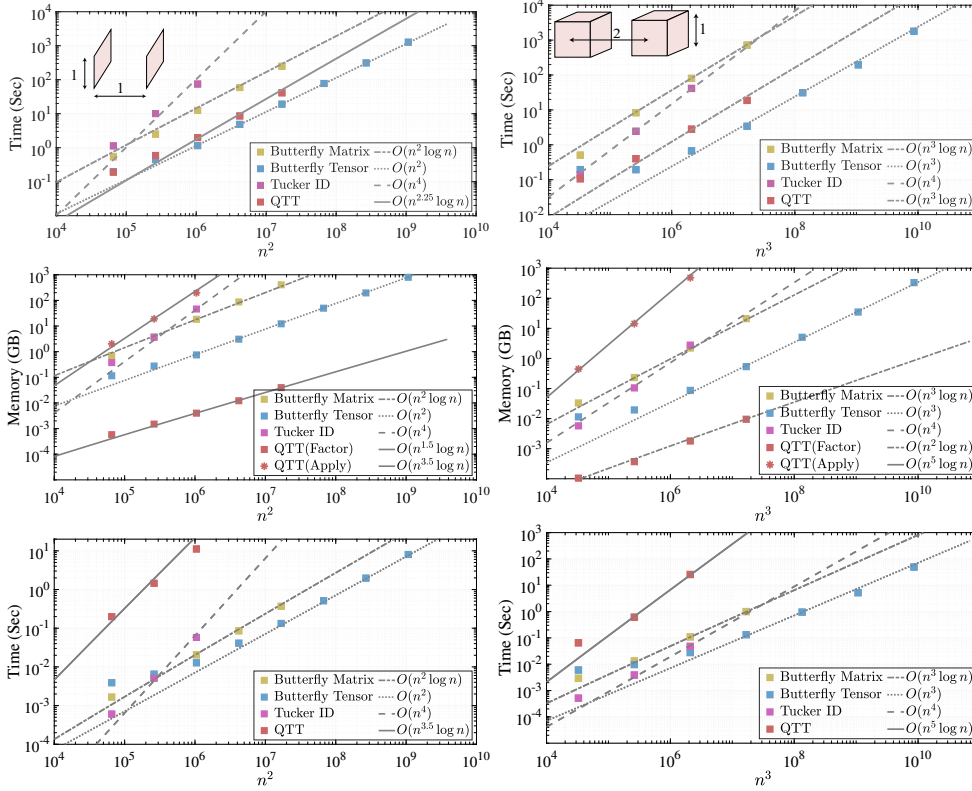


Fig. 4.1: Helmholtz equation: Computational complexity comparison among butterfly matrix, butterfly tensor, Tucker-ID and QTT for compressing (left) a 4-way Green's function tensor for interactions between two parallel 2D plates and (right) a 6-way Green's function tensor for interactions between two 3D cubes. The geometries are discretized with 4 points per wavelength. (Top): Factor time. (Middle): Factor and apply memory. (Bottom): Apply time. The largest data points correspond to 8192 wavelengths per direction for the 2D tests (left) and 512 wavelengths per direction for the 3D tests (right).

726 algorithm achieves a 30x memory reduction and 15x speedup, capable of handling 64x
 727 larger-sized tensors compared with the matrix butterfly algorithm.

728 **Figure 4.1** (right) shows the factorization time, application time and memory
 729 usage of each algorithm using a compression tolerance $\epsilon = 10^{-2}$ for the cube case.
 730 Overall, we achieve the expected complexities listed in **Table 3.1** for all four algorithms.
 731 The tensor butterfly algorithm achieves the linear CPU and memory complexities for
 732 both factorization and application with a much smaller prefactor compared to all the
 733 other algorithms. Remarkably, the tensor butterfly algorithm achieves a $30\times$ memory
 734 reduction and 200x speedup, capable of handling $512\times$ larger-sized tensors compared
 735 with the matrix butterfly algorithm. The largest data point $n = 2048$ corresponds
 736 to 512 wavelengths per physical dimension. The results in **Figure 4.1** suggest the
 737 superiority of the tensor butterfly algorithm in solving high-frequency wave equations
 738 in 3D volumes and on 3D surfaces.

739 Next, we demonstrate the effect of changing compression tolerance ϵ for both test

n^d	ϵ	r_{\min}	r	error	T_f (sec)	T_a (sec)	Mem (MB)
16384^2	1E-02	5	8	1.49E-02	6.83E+01	1.16E+00	2.40E+04
16384^2	1E-03	6	10	2.19E-03	1.17E+02	1.89E+00	4.69E+04
16384^2	1E-04	7	11	1.84E-04	1.57E+02	2.80E+00	7.49E+04
16384^2	1E-05	8	12	3.46E-05	2.29E+02	4.03E+00	1.21E+05
16384^2	1E-06	9	13	9.26E-06	3.18E+02	5.92E+00	1.96E+05
512^3	1E-02	2	5	2.01E-02	1.18E+02	1.42E+00	1.19E+04
512^3	1E-03	2	6	1.18E-03	3.46E+02	4.08E+00	4.87E+04
512^3	1E-04	2	7	8.39E-05	6.26E+02	9.85E+00	1.49E+05
512^3	1E-05	3	8	9.21E-06	1.25E+03	2.40E+01	4.07E+05

Table 4.1: The technical data for a 4-way Green’s function tensor of $n = 16384$ and a 6-way Green’s function tensor of $n = 512$ for the Helmholtz equation using the proposed tensor butterfly algorithm of varying compression tolerance ϵ . The table shows the maximum rank r and minimum rank r_{\min} across all ID operations, relative error in (4.2), factor time T_f , apply time T_a , and memory usage Mem .

740 cases in Table 4.1. Here the error is measured by

$$741 \quad (4.2) \quad \text{error} = \frac{\|\mathcal{K} \times_{d+1,d+2,\dots,2d} \mathcal{F}_e - \mathcal{K}_{BF} \times_{d+1,d+2,\dots,2d} \mathcal{F}_e\|_F}{\|\mathcal{K} \times_{d+1,d+2,\dots,2d} \mathcal{F}_e\|_F}$$

742 where \mathcal{K}_{BF} is the tensor butterfly representation of \mathcal{K} , $\mathcal{F}_e(\mathbf{j}) = 1$ for a small set of
743 random entries \mathbf{j} and 0 elsewhere. This way, \mathcal{K} does not need to be fully formed to
744 compute the error. Table 4.1 shows the minimum rank (r_{\min}) and maximum rank
745 (r), error, factorization time, application time and memory usage of varying ϵ , for
746 $n = 16384, d = 2$ and $n = 512, d = 3$. We remark that the observed ranks clearly
747 demonstrate $\Delta_\epsilon = O(\log \epsilon^{-1})$ in (3.18). Overall, the errors are close to the prescribed
748 tolerances and the costs increase for smaller ϵ , as expected. We also note that keeping
749 r as low as possible is critical in maintaining small prefactors of the tensor butterfly
750 algorithm, particularly for higher dimensions.

751 **4.2. Radon transforms.** In this subsection, we consider 2D and 3D discretized
752 Radon transforms similar to those presented in [8]. Specifically, the tensor entry is

$$753 \quad (4.3) \quad \mathcal{K}(\mathbf{i}, \mathbf{j}) = \exp(2\pi i \phi(x^{\mathbf{i}}, y^{\mathbf{j}}))$$

754 with $x^{\mathbf{i}} = (\frac{i_1}{n}, \frac{i_2}{n}, \dots, \frac{i_d}{n})$ and $y^{\mathbf{j}} = (j_1 - \frac{n}{2}, j_2 - \frac{n}{2}, \dots, j_d - \frac{n}{2})$. For $d = 2$, we consider

$$755 \quad (4.4) \quad \begin{aligned} \phi(x, y) &= x \cdot y + \sqrt{c_1^2 y_1^2 + c_2^2 y_2^2}, \\ 756 \quad c_1 &= (2 + \sin(2\pi x_1) \sin(2\pi x_2))/16, \\ 757 \quad c_2 &= (2 + \cos(2\pi x_1) \cos(2\pi x_2))/16. \end{aligned}$$

758 For $d = 3$, we consider

$$759 \quad (4.5) \quad \begin{aligned} \phi(x, y) &= x \cdot y + c|y|, \\ 760 \quad c &= (3 + \sin(2\pi x_1) \sin(2\pi x_2) \sin(2\pi x_3))/100. \end{aligned}$$

761 We first perform compression using the matrix butterfly, tensor butterfly, and QTT
762 algorithms, and then perform application/contraction using a random input tensor
763 \mathcal{F} .

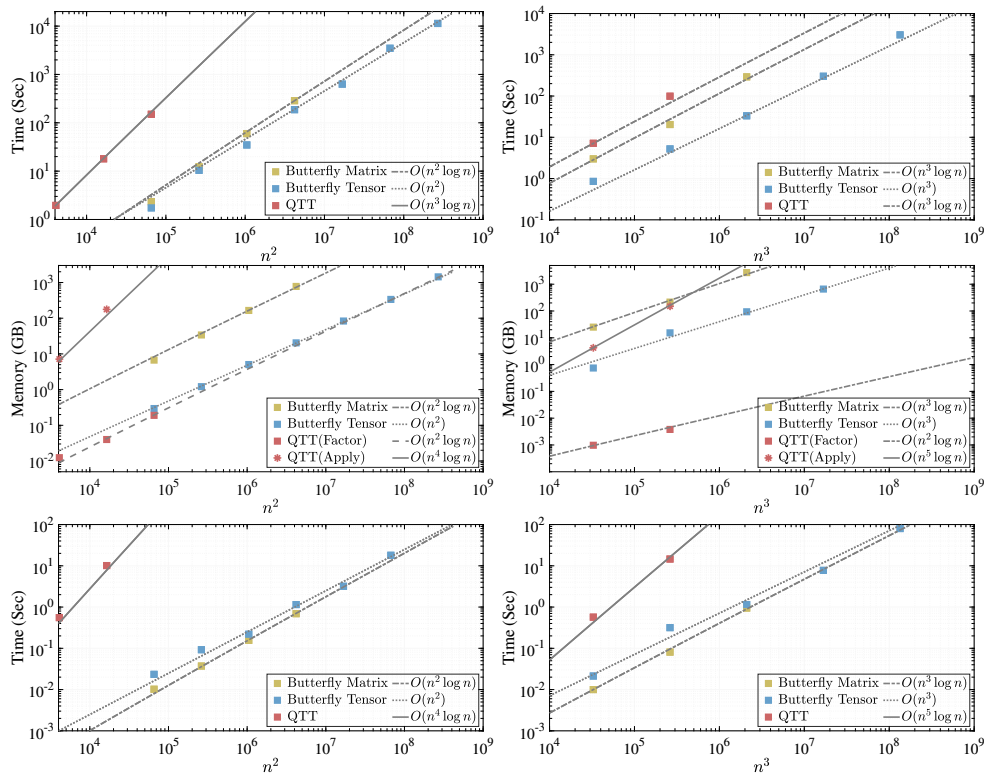


Fig. 4.2: Radon transforms: Computational complexity comparison among butterfly matrix, butterfly tensor and QTT for compressing (left) a 2D Radon transform tensor and (right) a 3D Radon transform tensor. (Top): Factor time. (Middle): Factor and apply memory. (Bottom): Apply time.

764 Figure 4.2 shows the factorization time, application time and memory usage of
765 each algorithm using a compression tolerance $\epsilon = 10^{-3}$ for the 2D transform (left)
766 and 3D transform (right). Overall, we achieve the expected complexities listed in
767 Table 3.1 for all three algorithms. The QTT algorithm can only obtain the first 2 or
768 3 data points due to its high memory usage and large QTT ranks. In comparison,
769 the tensor butterfly algorithm achieves the linear CPU and memory complexities for
770 both factorization and application with a much smaller prefactor compared to all
771 the other algorithms. Note that the Radon transform kernels in (4.4) and (4.5) are
772 not translational invariant, but the tensor butterfly algorithm can still attain small
773 ranks. As a result, the tensor butterfly algorithm can handle 64x larger-sized Radon
774 transforms compared with the matrix butterfly algorithm, showing their superiority
775 for solving linear inverse problems in tomography and seismic imaging.

776 Next, we demonstrate the effect of changing compression tolerance ϵ for both test
777 cases in Table 4.2 with the error defined by (4.2). Table 4.2 shows the minimum
778 and maximum ranks, error, factorization time, application time and memory usage
779 of varying ϵ , for $n = 2048$ with $d = 2$ and $n = 128$ with $d = 3$, respectively. Overall,
780 the errors are close to the prescribed tolerances and the costs increase for smaller ϵ ,
781 as expected. Just like the Green's function example, it is critical to keep r a low
782 constant, particularly for higher dimensions.

n^d	ϵ	r_{\min}	r	error	$T_f(\text{sec})$	$T_a(\text{sec})$	Mem (MB)
2048 ²	1E-02	4	18	2.04E-02	9.32E+01	7.20E-01	1.25E+04
2048 ²	1E-03	4	20	1.51E-03	1.61E+02	1.28E+00	2.40E+04
2048 ²	1E-04	4	22	1.49E-04	2.55E+02	2.05E+00	4.26E+04
2048 ²	1E-05	4	23	2.45E-05	3.73E+02	3.12E+00	6.95E+04
128 ³	1E-02	2	6	4.31E-02	3.89E+01	8.57E-01	1.59E+04
128 ³	1E-03	2	8	1.00E-02	1.31E+02	3.74E+00	9.44E+04
128 ³	1E-04	2	9	1.68E-03	2.42E+02	8.28E+00	2.38E+05
128 ³	1E-05	2	11	1.48E-04	4.30E+02	2.05E+01	6.06E+05

Table 4.2: The technical data for a 4-way Radon transform tensor of $n = 2048$ in (4.4) and a 6-way Radon transform tensor of $n = 128$ in (4.5) using the proposed tensor butterfly algorithm of varying compression tolerance ϵ . The table shows the maximum rank r and minimum rank r_{\min} across all ID operations, relative error in (4.2), factor time T_f , apply time T_a , and memory usage Mem .

783 **4.3. High-dimensional discrete Fourier transform.** Finally, we consider
784 high-dimensional DFTs defined as

$$785 \quad (4.6) \quad \mathcal{K}(\mathbf{i}, \mathbf{j}) = \exp(2\pi i \mathbf{x}^{\mathbf{i}} \cdot \mathbf{y}^{\mathbf{j}}),$$

786 where we choose $\mathbf{x}^{\mathbf{i}} = (i_1 - 1, i_2 - 1, \dots, i_d - 1)$ and $\mathbf{y}^{\mathbf{j}} = (\frac{j_1-1}{n}, \frac{j_2-1}{n}, \dots, \frac{j_d-1}{n})$ for
787 uniform DFTs, and we choose $\mathbf{x}^{\mathbf{i}}$ to be random (in the sense that $x_k^{\mathbf{i}} \in [0, n - 1]$ for
788 $k \leq d$ is a random number) and $\mathbf{y}^{\mathbf{j}} = (\frac{j_1-1}{n}, \frac{j_2-1}{n}, \dots, \frac{j_d-1}{n})$ for type-2 non-uniform
789 DFTs. For high-dimensional DFTs with $d = 3, 4, 5, 6$, we perform compression using
790 the tensor butterfly algorithms (with the bit-reversal ordering for each dimension),
791 and perform application/contraction using a random input tensor \mathcal{F} . In comparison,
792 for $d = 3$ we perform FFT via the heFFTe package for the uniform DFT example and
793 NUFFT via the FINUFFT package for the type-2 non-uniform DFT example.

794 Figure 4.3 shows the factorization time for the butterfly algorithm (or equiva-
795 lently the plan creation time for heFFTe/FINUFFT), application time and memory
796 usage of each algorithm using a compression tolerance $\epsilon = 10^{-3}$ (for butterfly and
797 FINUFFT) for the uniform (left) and nonuniform (right) transforms. Overall, the ten-
798 sor butterfly algorithm can obtain $O(n^d)$ CPU and memory complexities compared
799 with the $O(n^d \log n)$ complexities of FFT and NUFFT. It is also worth mentioning
800 that QTT can attain logarithmic-complexity uniform DFTs [9] when the input tensor
801 \mathcal{F} is also in the QTT form with low TT ranks. However, for a general input ten-
802 sor, the complexity of QTT falls back to $O(n^d \log n)$. Although the proposed tensor
803 butterfly algorithm can obtain the best computational complexity among all existing
804 algorithms, we observe that for the $d = 3$ case, FFT or NUFFT shows a memory
805 usage similar to the tensor butterfly algorithm but much smaller prefactors for plan
806 creation and application time. That said, the tensor butterfly algorithm provides
807 a unique capability to perform higher dimensional DFTs (i.e., $d \geq 4$) with optimal
808 asymptotic complexities.

809 **5. Conclusion.** We present a new tensor butterfly algorithm efficiently com-
810 pressing and applying large-scale and high-dimensional OIOs, such as Green’s func-
811 tions for wave equations and integral transforms, including Radon transforms and
812 Fourier transforms. The tensor butterfly algorithm leverages an essential tensor CLR

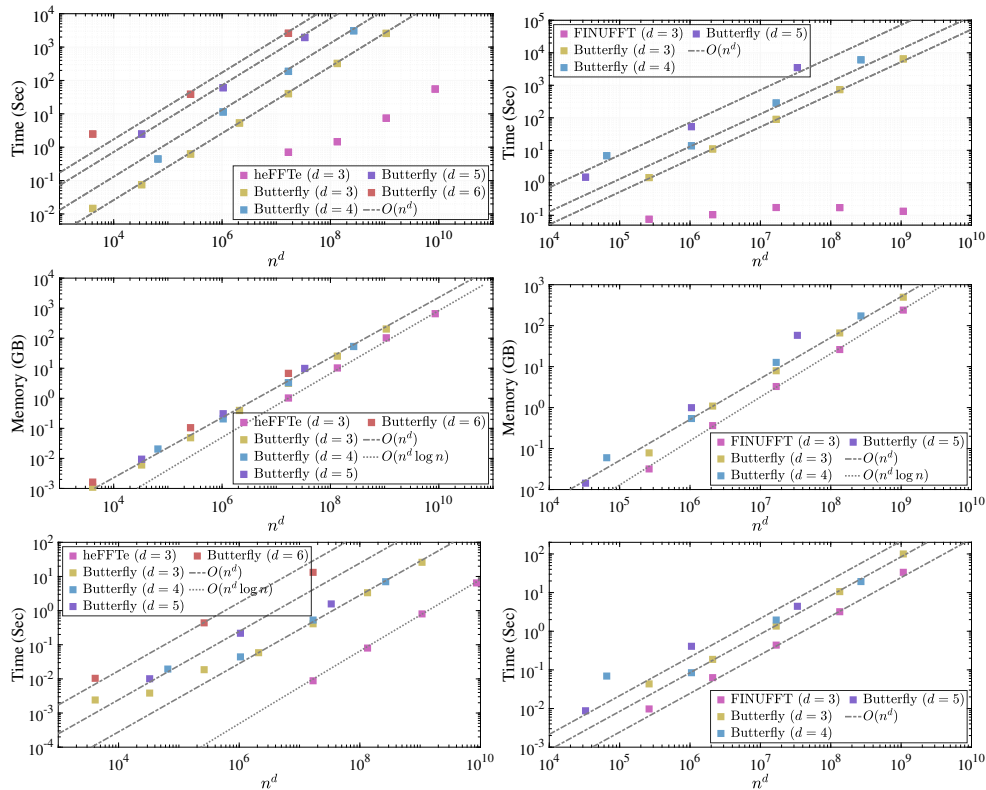


Fig. 4.3: Fourier transforms: Computational complexity of (left) butterfly tensor and heFFTe for compressing the high-dimensional DFT tensor and (right) butterfly tensor and FINUFFT for compressing the high-dimensional NUFFT tensor. (Top): Factor time of butterfly tensor and plan creation time for heFFTe/FINUFFT. (Middle): Factor memory. (Bottom): Apply time.

813 property to achieve both improved asymptotic computational complexities and lower
 814 leading constants. For the contraction of high-dimensional OIOs with arbitrary input
 815 tensors, the tensor butterfly algorithm achieves the optimal linear CPU and memory
 816 complexities; this is in huge contrast with both existing matrix algorithms and fast
 817 transform algorithms. The former includes the matrix butterfly algorithm, and the
 818 latter contains FFT, NUFFT, and other tensor algorithms such as Tucker-type de-
 819 compositions and QTT. Nevertheless, all these algorithms exhibit higher asymptotic
 820 complexities and larger leading constants. As a result, the tensor butterfly algorithm
 821 can efficiently model high-frequency 3D Green’s function interactions with over $512\times$
 822 larger problem sizes than existing butterfly algorithms; for the largest sized tensor
 823 that can be handled by existing algorithms, the tensor butterfly algorithm requires
 824 $200\times$ less CPU time and $30\times$ less memory than existing algorithms. Moreover, it
 825 can perform linear-complexity Radon transforms and DFTs with up to $d = 6$ di-
 826 mensions. These OIOs are frequently encountered in the solution of high-frequency
 827 wave equations, X-ray and MRI-based inverse problems, seismic imaging and signal
 828 processing; therefore, we expect the tensor butterfly algorithm developed here to be
 829 both theoretically attractive and practically useful for many applications.

830 The limitation of the tensor butterfly algorithm is the requirement for a tensor

831 grid, and hence its extension for unstructured meshes will be a future work. Also, the
832 mid-level subtensors represent a memory bottleneck and need to be compressed with
833 more efficient algorithms.

834 **Acknowledgements.** This research has been supported by the U.S. Depart-
835 ment of Energy, Office of Science, Office of Advanced Scientific Computing Research,
836 Mathematical Multifaceted Integrated Capability Centers (MMICCs) program, under
837 Contract No. DE-AC02-05CH11231 at Lawrence Berkeley National Laboratory. This
838 work was also supported in part by the NSF Mathematical Sciences Graduate In-
839 ternship (NSF MSGI) program. This research used resources of the National Energy
840 Research Scientific Computing Center, a DOE Office of Science User Facility sup-
841 ported by the Office of Science of the U.S. Department of Energy under Contract No.
842 DE-AC02-05CH11231 using NERSC award ASCR-ERCAP0024170. Qian’s research
843 was partially supported by NSF grants 2152011 and 2309534 and an MSU SPG grant.

844

REFERENCES

- 845 [1] Alan Ayala, Stanimire Tomov, Piotr Luszczek, Sebastien Cayrols, Gerald Ragghianti, and Jack
846 Dongarra. Analysis of the communication and computation cost of FFT libraries towards
847 exascale. Technical Report ICL-UT-22-07, 2022-07 2022.
- 848 [2] Alexander H Barnett, Jeremy Magland, and Ludvig af Klinteberg. A parallel nonuniform fast
849 Fourier transform library based on an “exponential of semicircle” kernel. *SIAM J. Sci.*
850 *Comput.*, 41(5):C479–C504, 2019.
- 851 [3] David Joseph Biagioni. *Numerical construction of Green’s functions in high dimensional elliptic*
852 *problems with variable coefficients and analysis of renewable energy data via sparse and*
853 *separable approximations*. PhD thesis, University of Colorado at Boulder, 2012.
- 854 [4] James Bremer, Ze Chen, and Haizhao Yang. Rapid application of the spherical harmonic
855 transform via interpolative decomposition butterfly factorization. *SIAM J. Sci. Comput.*,
856 43(6):A3789–A3808, 2021.
- 857 [5] Ovidio M Bucci and Giorgio Franceschetti. On the degrees of freedom of scattered fields. *IEEE*
858 *Trans. Antennas Propagat.*, 37(7):918–926, 1989.
- 859 [6] HanQin Cai, Keaton Hamm, Longxiu Huang, and Deanna Needell. Mode-wise tensor decom-
860 positions: Multi-dimensional generalizations of cur decompositions. *J. Mach. Learn. Res.*,
861 22(185):1–36, 2021.
- 862 [7] Emmanuel Candes, Laurent Demanet, and Lexing Ying. Fast computation of Fourier integral
863 operators. *SIAM J. Sci. Comput.*, 29(6):2464–2493, 2007.
- 864 [8] Emmanuel Candès, Laurent Demanet, and Lexing Ying. A fast butterfly algorithm for the
865 computation of Fourier integral operators. *SIAM Multiscale Model. Simul.*, 7(4):1727–
866 1750, 2009.
- 867 [9] Jielun Chen and Michael Lindsey. Direct interpolative construction of the discrete Fourier
868 transform as a matrix product operator. *arXiv preprint arXiv:2404.03182*, 2024.
- 869 [10] Ze Chen, Juan Zhang, Kenneth L Ho, and Haizhao Yang. Multidimensional phase recovery and
870 interpolative decomposition butterfly factorization. *J. Comput. Phys.*, 412:109427, 2020.
- 871 [11] Jian Cheng, Dinggang Shen, Peter J Basser, and Pew-Thian Yap. Joint 6D kq space compressed
872 sensing for accelerated high angular resolution diffusion MRI. In *Information Processing*
873 *in Medical Imaging: 24th International Conference, IPMI 2015, Sabhal Mor Ostaig, Isle*
874 *of Skye, UK, June 28-July 3, 2015, Proceedings*, pages 782–793. Springer, 2015.
- 875 [12] Andrzej Cichocki, Namgil Lee, Ivan Oseledets, Anh-Huy Phan, Qibin Zhao, Danilo P Mandic,
876 et al. Tensor networks for dimensionality reduction and large-scale optimization: Part 1
877 low-rank tensor decompositions. *Found. Trends Mach. Learn.*, 9(4-5):249–429, 2016.
- 878 [13] Lisa Claus, Pieter Ghysels, Yang Liu, Thái Anh Nhan, Ramakrishnan Thirumalaisamy, Am-
879 neet Pal Singh Bhalla, and Sherry Li. Sparse approximate multifrontal factorization with
880 composite compression methods. *ACM Trans. Math. Softw.*, 49(3):1–28, 2023.
- 881 [14] Eduardo Corona, Abtin Rahimian, and Denis Zorin. A tensor-train accelerated solver for
882 integral equations in complex geometries. *J. Comput. Phys.*, 334:145–169, 2017.
- 883 [15] Maurice A De Gosson. *The Wigner Transform*. World Scientific Publishing Company, 2017.
- 884 [16] Lieven De Lathauwer, Bart De Moor, and Joos Vandewalle. A multilinear singular value
885 decomposition. *SIAM J. Matrix Anal. Appl.*, 21(4):1253–1278, 2000.
- 886 [17] Stanley R Deans. *The Radon transform and some of its applications*. Courier Corporation,

- 887 2007.
- 888 [18] Gian Luca Delzanno. Multi-dimensional, fully-implicit, spectral method for the Vlasov–Maxwell
889 equations with exact conservation laws in discrete form. *J. Comput. Phys.*, 301:338–356,
890 2015.
- 891 [19] Sergey Dolgov and Dmitry Savostyanov. Parallel cross interpolation for high-precision calcula-
892 tion of high-dimensional integrals. *Comput. Phys. Commun. Communications*, 246:106869,
893 2020.
- 894 [20] Björn Engquist and Lexing Ying. Fast directional multilevel algorithms for oscillatory kernels.
895 *SIAM J. Sci. Comput.*, 29(4):1710–1737, 2007.
- 896 [21] Alexander L Fetter and John Dirk Walecka. *Quantum theory of many-particle systems*. Courier
897 Corporation, 2012.
- 898 [22] Ilias I Giannakopoulos, Mikhail S Litsarev, and Athanasios G Polimeridis. Memory footprint
899 reduction for the FFT-based volume integral equation method via tensor decompositions.
900 *IEEE Trans. Antennas Propagat.*, 67(12):7476–7486, 2019.
- 901 [23] Lars Grasedyck, Daniel Kressner, and Christine Tobler. A literature survey of low-rank tensor
902 approximation techniques. *GAMM-Mitteilungen*, 36(1):53–78, 2013.
- 903 [24] Han Guo, Jun Hu, and Eric Michielssen. On MLMDA/butterfly compressibility of inverse
904 integral operators. *IEEE Antennas Wirel. Propag. Lett.*, 12:31–34, 2013.
- 905 [25] Han Guo, Yang Liu, Jun Hu, and Eric Michielssen. A butterfly-based direct integral-equation
906 solver using hierarchical LU factorization for analyzing scattering from electrically large
907 conducting objects. *IEEE Trans. Antennas Propag.*, 65(9):4742–4750, 2017.
- 908 [26] Han Guo, Yang Liu, Jun Hu, and Eric Michielssen. A butterfly-based direct solver using hier-
909 archical LU factorization for Poggio-Miller-Chang-Harrington-Wu-Tsai equations. *Microw
910 Opt Technol Lett.*, 60:1381–1387, 2018.
- 911 [27] Wolfgang Hackbusch and Boris N Khoromskij. Tensor-product approximation to multidimen-
912 sional integral operators and Green’s functions. *SIAM J. Matrix Anal. Appl.*, 30(3):1233–
913 1253, 2008.
- 914 [28] Wolfgang Hackbusch and Stefan Kühn. A new scheme for the tensor representation. *J. Fourier
915 Anal. Appl.*, 15(5):706–722, 2009.
- 916 [29] Nathan Halko, Per-Gunnar Martinsson, and Joel A. Tropp. Finding structure with random-
917 ness: probabilistic algorithms for constructing approximate matrix decompositions. *SIAM
918 Review*, 53(2):217–288, January 2011.
- 919 [30] Richard A Harshman et al. Foundations of the PARAFAC procedure: Models and conditions
920 for an “explanatory” multi-modal factor analysis. *UCLA working papers in phonetics*,
921 16(1):84, 1970.
- 922 [31] Rui Hong, Ya-Xuan Xiao, Jie Hu, An-Chun Ji, and Shi-Ju Ran. Functional tensor network
923 solving many-body Schrödinger equation. *Phys. Rev. B*, 105:165116, Apr 2022.
- 924 [32] L Hörmander. Fourier integral operators. i. In *Mathematics Past and Present Fourier Integral
925 Operators*, pages 23–127. Springer, 1994.
- 926 [33] Yuehaw Khoo and Lexing Ying. Switchnet: a neural network model for forward and inverse
927 scattering problems. *SIAM J. Sci. Comput.*, 41(5):A3182–A3201, 2019.
- 928 [34] Tamara G Kolda and Brett W Bader. Tensor decompositions and applications. *SIAM review*,
929 51(3):455–500, 2009.
- 930 [35] Matthew Li, Laurent Demanet, and Leonardo Zepeda-Núñez. Wide-band butterfly network:
931 stable and efficient inversion via multi-frequency neural networks. *SIAM Multiscale Model.
932 Simul.*, 20(4):1191–1227, 2022.
- 933 [36] Yingzhou Li and Haizhao Yang. Interpolative butterfly factorization. *SIAM J. Sci. Comput.*,
934 39(2):A503–A531, 2017.
- 935 [37] Yingzhou Li, Haizhao Yang, Eileen R Martin, Kenneth L Ho, and Lexing Ying. Butterfly
936 factorization. *SIAM Multiscale Model. Simul.*, 13(2):714–732, 2015.
- 937 [38] Yingzhou Li, Haizhao Yang, and Lexing Ying. Multidimensional butterfly factorization. *Appl.
938 Comput. Harmon. Anal.*, 44(3):737–758, 2018.
- 939 [39] E. Liberty, F. Woolfe, P.-G. Martinsson, V. Rokhlin, and M. Tygert. Randomized algorithms
940 for the low-rank approximation of matrices. *Proc. Natl. Acad. Sci. USA*, 104:20167–20172,
941 2007.
- 942 [40] Peter Lindstrom. Fixed-rate compressed floating-point arrays. *IEEE Trans. Vis. Comput.
943 Graph.*, 20(12):2674–2683, 2014.
- 944 [41] Yang Liu. A comparative study of butterfly-enhanced direct integral and differential equation
945 solvers for high-frequency electromagnetic analysis involving inhomogeneous dielectrics. In
946 *2022 3rd URSI Atlantic and Asia Pacific Radio Science Meeting (AT-AP-RASC)*, pages
947 1–4. IEEE, 2022.
- 948 [42] Yang Liu, Pieter Ghysels, Lisa Claus, and Xiaoye Sherry Li. Sparse approximate multifrontal

- 949 factorization with butterfly compression for high-frequency wave equations. *SIAM J. Sci.*
950 *Comput.*, 0(0):S367–S391, 2021.
- 951 [43] Yang Liu, Han Guo, and Eric Michielssen. An HSS matrix-inspired butterfly-based direct solver
952 for analyzing scattering from two-dimensional objects. *IEEE Antennas Wirel. Propag.*
953 *Lett.*, 16:1179–1183, 2017.
- 954 [44] Yang Liu, Tianhuan Luo, Aman Rani, Hengrui Luo, and Xiaoye Sherry Li. Detecting reso-
955 nance of radio-frequency cavities using fast direct integral equation solvers and augmented
956 Bayesian optimization. *IEEE J. Multiscale Multiphysics Comput. Tech.*, 2023.
- 957 [45] Yang Liu, Jian Song, Robert Burrige, and Jianliang Qian. A fast butterfly-compressed
958 Hadamard-Babich integrator for high-frequency Helmholtz equations in inhomogeneous
959 media with arbitrary sources. *SIAM Multiscale Model. Simul.*, 21(1):269–308, 2023.
- 960 [46] Yang Liu and USDOE. ButterflyPACK, 11 2018. URL: [https://github.com/liuyangzhuang/](https://github.com/liuyangzhuang/ButterflyPACK)
961 [ButterflyPACK](https://github.com/liuyangzhuang/ButterflyPACK).
- 962 [47] Yang Liu, Xin Xing, Han Guo, Eric Michielssen, Pieter Ghysels, and Xiaoye Sherry Li. But-
963 teryfly factorization via randomized matrix-vector multiplications. *SIAM J. Sci. Comput.*,
964 43(2):A883–A907, 2021.
- 965 [48] Yang Liu and Haizhao Yang. A hierarchical butterfly LU preconditioner for two-dimensional
966 electromagnetic scattering problems involving open surfaces. *J. Comput. Phys.*,
967 401:109014, 2020.
- 968 [49] W. Lu, J. Qian, and R. Burrige. Babich’s expansion and the fast Huygens sweeping method
969 for the Helmholtz wave equation at high frequencies. *J. Comput. Phys.*, 313:478–510, 2016.
- 970 [50] Axel Maas. Two and three-point Green’s functions in two-dimensional Landau-gauge Yang-
971 Mills theory. *Phys. Rev. D*, 75:116004, 2007.
- 972 [51] Michael W Mahoney, Mauro Maggioni, and Petros Drineas. Tensor-CUR decompositions for
973 tensor-based data. In *Proceedings of the 12th ACM SIGKDD international conference on*
974 *Knowledge discovery and data mining*, pages 327–336, 2006.
- 975 [52] Osman Asif Malik and Stephen Becker. Fast randomized matrix and tensor interpolative de-
976 composition using counts sketch. *Adv. Comput. Math.*, 46(6):76, 2020.
- 977 [53] Eric Michielssen and Amir Boag. Multilevel evaluation of electromagnetic fields for the rapid
978 solution of scattering problems. *Microw Opt Technol Lett.*, 7(17):790–795, 1994.
- 979 [54] Eric Michielssen and Amir Boag. A multilevel matrix decomposition algorithm for analyzing
980 scattering from large structures. *IEEE Trans. Antennas Propag.*, 44(8):1086–1093, 1996.
- 981 [55] Rachel Minster, Arvind K Saibaba, and Misha E Kilmer. Randomized algorithms for low-
982 rank tensor decompositions in the Tucker format. *SIAM journal on mathematics of data*
983 *science*, 2(1):189–215, 2020.
- 984 [56] Michael O’Neil, Franco Woolfe, and Vladimir Rokhlin. An algorithm for the rapid evaluation
985 of special function transforms. *Appl. Comput. Harmon. A.*, 28(2):203 – 226, 2010. Special
986 Issue on Continuous Wavelet Transform in Memory of Jean Morlet, Part I.
- 987 [57] Ivan V Oseledets. Tensor-train decomposition. *SIAM J. Sci. Comput.*, 33(5):2295–2317, 2011.
- 988 [58] Qiyuan Pang, Kenneth L. Ho, and Haizhao Yang. Interpolative decomposition butterfly fac-
989 torization. *SIAM J. Sci. Comput.*, 42(2):A1097–A1115, 2020.
- 990 [59] Michael E Peskin. *An introduction to quantum field theory*. CRC press, 2018.
- 991 [60] Arvind K Saibaba. HOID: higher order interpolatory decomposition for tensors based on Tucker
992 representation. *SIAM J. Matrix Anal. Appl.*, 37(3):1223–1249, 2016.
- 993 [61] Sadeed Bin Sayed, Yang Liu, Luis J. Gomez, and Abdulkadir C. Yucel. A butterfly-accelerated
994 volume integral equation solver for broad permittivity and large-scale electromagnetic
995 analysis. *IEEE Trans. Antennas Propagat.*, 70(5):3549–3559, 2022.
- 996 [62] Weitian Sheng, Abdulkadir C Yucel, Yang Liu, Han Guo, and Eric Michielssen. A domain
997 decomposition based surface integral equation simulator for characterizing EM wave prop-
998 agation in mine environments. *IEEE Trans. Antennas Propagat.*, 2023.
- 999 [63] Tianyi Shi, Daniel Hayes, and Jing-Mei Qiu. Distributed memory parallel adaptive tensor-train
1000 cross approximation. *arXiv preprint arXiv:2407.11290*, 2024.
- 1001 [64] Edgar Solomonik, Devin Matthews, Jeff Hammond, and James Demmel. Cyclops tensor frame-
1002 work: Reducing communication and eliminating load imbalance in massively parallel con-
1003 tractions. In *2013 IEEE 27th International Symposium on Parallel and Distributed Pro-*
1004 *cessing*, pages 813–824. IEEE, 2013.
- 1005 [65] Mark Tygert. Fast algorithms for spherical harmonic expansions, III. *J. Comput. Phys.*,
1006 229(18):6181 – 6192, 2010.
- 1007 [66] Mingyu Wang, Cheng Qian, Enrico Di Lorenzo, Luis J Gomez, Vladimir Okhmatovski, and Ab-
1008 dulkadir C Yucel. SuperVoxHenry: Tucker-enhanced and FFT-accelerated inductance ex-
1009 traction for voxelized superconducting structures. *IEEE Trans. Appl. Supercond.*, 31(7):1–
1010 11, 2021.

1011 [67] Mingyu Wang, Cheng Qian, Jacob K White, and Abdulkadir C Yucel. VoxCap: FFT-
1012 accelerated and Tucker-enhanced capacitance extraction simulator for voxelized structures.
1013 *IEEE Trans. Microw. Theory Tech.*, 68(12):5154–5168, 2020.

1014 [68] E. Wigner. On the quantum correction for thermodynamic equilibrium. *Phys. Rev.*, 40:749–759,
1015 Jun 1932.

1016 [69] Haizhao Yang. A unified framework for oscillatory integral transforms: When to use NUFFT
1017 or butterfly factorization? *J. Comput. Phys.*, 388:103 – 122, 2019.

1018 [70] Lexing Ying. Sparse Fourier transform via butterfly algorithm. *SIAM J. Sci. Comput.*,
1019 31(3):1678–1694, 2009.